ETH
Eidgenössische Technische Hochschule Zürich
Swiss Federal Institute of Technology Zurich

Master's Thesis

Towards the realization of a transmon longitudinally coupled to a lumped element resonator

Adrian Beckert

Supervisor:
Theodore E. Walter

Professor:
Prof. Dr. Andreas Wallraff

April 21, 2016

Abstract

This thesis presents experimental work towards the design and measurement of a transmon longitudinally coupled to a lumped element resonator. First, the performance and characteristics of lumped element resonators with a Josephson junction array inductor were tested. Second, a circuit realization recently proposed by N.Didier *et al.* was experimentally examined. This realization was found not to provide the desired longitudinal coupling, but showed strong transversal coupling instead. The failure of the circuit realization could be attributed to the asymmetric shunting of the qubit Josephson junctions. Furthermore, the experiments revealed the problem of the resonator tunability which is closely related to the inductance ratio of the resonator to the qubit and raised the question of how and where the ground has to be placed in order to enable a longitudinal qubit-resonator coupling.
These results have lead to a new insights for a design which is expected to exhibit the desired strong longitudinal properties.

Contents

1.Introduction and Motivation

Circuit Quantum Electro Dynamics (cQED) is currently one of the most promising ways to realize a scalable quantum computer. Since its theoretical proposition in 1980 [1] collective degree of freedom tunneling in Josephson junctions [2] has been observed as well as coherent single qubit oscillations [3]. This led to the demonstration of artificial atoms with larger decoherence times [4–7] and subsequent entanglement of two or more of them [8–10]. These artificial atoms, serving as qubits, were subsequently used to demonstrate quantum algorithms [11–13] and quantum error correction [14].
All the recent results in cQED towards a scalable quantum computer relied on dispersive qubit readout. Dispersive qubit readout utilizes a qubit state dependent frequency shift of a transversally coupled resonator. This qubit state dependent frequency shift can be resolved by homodyne detection [15, 16]. Although widely used, this readout method is only quantum non demolition (QND) in a perturbative sense and is thus afflicted with several disadvantages such as photon lifetime dependent qubit relaxation times, known as Purcell decay [17].
If the qubit is coupled longitudinally to the resonator, instead of transversally with respect to its quantization direction, a fundamentally different situation arises. This approach was first applied to trapped ions [18–22] and was recently proposed for cQED [23, 24]. This thesis provides experimental work towards a realization of longitudinal qubit readout, proposed by N.Didier *et al.* [25], which avoids most of the disadvantages of dispersive readout and has several advantages. For example, this type of coupling does not cause Purcell decay of the qubit through the resonator, nor is the measurement a perturbatively QND. Thus large measurement power can be used. Also, the measurement operator leads to a more ideal separation of the quibt state dependent field allowing for faster measurement speeds. Finally, this type of readout could see an exponential improvement of the SNR by using squeezed input states, a feature unobtainable for dispersive readout.

2.Theoretic fundamentals

2.1. Transversal and longitudinal coupling

2.1.1. Introduction

Some general considerations about the difference between longitudinal and transversal coupling are discussed below.
Transversal and longitudinal coupling refer to the degrees of freedom through which the qubit couples to the resonator. Transversal refers to interactions of the qubit perpendicular to its quantization axis, while longitudinal is parallel to this axis. Typically, the quantization axis is denoted the z-axis, making transversal an x or y and longitudinal a z, interaction. The difference can not be seen directly by considering an electric circuit diagram, although ref. [23] demonstrates some intuition for how electrical circuits can be rotated by 90^o to change the coupling from a transversal to a longitudinal nature. For general cases a thorough circuit quantization following [26] and Hamiltonian diagonalization has to be done in order to determine the kind of coupling terms present in a circuit. There is always a transversal and a longitudinal coupling present and the question of which one dominates the system crucially depends not only on the circuit topology, but also on the circuit parameters. A profound discussion of the differences of transversal and longitudinal coupling and its (dis)advantages can be found in reference [24].
In a nutshell, the fundamental difference between the transversal and longitudinal coupling consists of the qubit degree of freedom to which the resonator couples.

2.1.2. Transversal coupling Hamiltonian

This section briefly treats the Hamiltonian of a transversal qubit-resonator coupling and its diagonalization.
The Hamiltonian describing the transversal interaction of a resonator and a qubit (two-level system) is called the Jaynes-Cummings Hamiltonian [27] and reads in the interaction picture as follows

$$\mathcal{H} = \omega_\mathrm{r}\left(a^\dagger a\right) + \frac{\omega_\mathrm{q}}{2}\sigma_\mathrm{z} + g_\mathrm{x}\sigma_\mathrm{x}(a^\dagger + a) \tag{2.1}$$

where ω_r denotes the resonator frequency, ω_q the qubit energy gap between the $|0\rangle$ and the $|1\rangle$ state and g_x the transversal coupling between the qubit and the resonator. If the detuning Δ of the resonator to the qubit is much larger than the coupling g_x, i.e.$|\omega_\mathrm{r} - \omega_\mathrm{q}| = \Delta \gg g_\mathrm{x}$ the Hamiltonian in Eq. (2.1) can be approximately diagonalized to

$$\mathcal{H} = \omega_\mathrm{r}\left(a^\dagger a\right) + \frac{\omega_\mathrm{q}}{2}\sigma_\mathrm{z} + \chi\sigma_\mathrm{z}(a^\dagger + a) \tag{2.2}$$

where χ denotes the dispersive shift exploited by the dispersive qubit readout. However the Hamiltonian of Eq. (2.1) was just approximately diagonalized, the derived energies are not

the true eigenenergies of the Hamiltonians eigenstates. Thus, the dispersive readout is not a QND measurement. This non-QNDness negatively impacts the qubit coherence time and leads to qubit state measurement errors due to mixing of the computational states [23].
The problems of transversal coupling are a direct consequence that the Hamiltonian can only be approximately diagonalized which therefore leads to several disadvantages.

2.1.3. Longitudinal coupling Hamiltonian

In contrast to the transversal coupling Hamiltonian, a longitudinal coupling Hamiltonian is briefly studied in this section.
The Hamiltonian coupling a qubit longitudinally to a resonator is given by

$$\mathcal{H} = \omega_\mathrm{r} a^\dagger a + \frac{\omega_\mathrm{q}}{2}\sigma_\mathrm{z} + g_\mathrm{z}\sigma_\mathrm{z}\left(a + a^\dagger\right) \tag{2.3}$$

with the resonator frequency ω_r, the qubit resonance frequency ω_q and the qubit-oscillator coupling strength g_z. Contrary to the transversal case shown in Eq. (2.1), the Hamiltonian for the longitudinal coupling in Eq. (2.3) exhibits a σ_z operator instead of a σ_x operator in the coupling term. Following [24], Eq. (2.3) can be diagonalized using a Lang-Firsov transformation. The transformation matrix U reads

$$U = \exp\left[-\frac{g_\mathrm{z}}{\omega_\mathrm{r}}\sigma_\mathrm{z}\left(a^\dagger - a\right)\right] \tag{2.4}$$

and maps the Hamiltonian of Eq. (2.3) into

$$\mathcal{H}' = \omega_\mathrm{r} a^\dagger a + \frac{\omega_\mathrm{q}}{2}\sigma_\mathrm{z} + \frac{g_\mathrm{z}^2}{\omega_\mathrm{r}}\mathbb{1} \tag{2.5}$$

. Two important observations can be made: First, the Lang-Firsov transformation is exact and did not renormalize the resonator or qubit frequency, but only the zero point energy. Second, whether the qubit is in the ground state or not, there is no interaction with the resonator and thus no dispersive shift of the resonator frequency due to the absence of a $\sigma_\mathrm{z}(a^\dagger + a)$ term. The pure QND nature of the longitudinal coupling is the reason why this type of coupling avoids Purcell decay [23, 24].
The benefit of longitudinal coupling derives from this: The exact diagonalization which avoids the admixture of non-eigenstates when the system is measured since the Hamiltonian truly commutes with the σ_z measurement operator. The absence of the $\sigma_\mathrm{z}(a^\dagger + a)$ term avoids a constant qubit-resonator interaction and therefore entanglement between the two subsystems. However, the constant qubit-resonator interaction in the transversal case is useful for qubit state readout whereas in the longitudinal case a different approach has to be applied.
In summary the longitudinal coupling provides a few advantages over the transversal coupling due to its QND nature although the absence of a dispersive shift complicates the qubit readout.

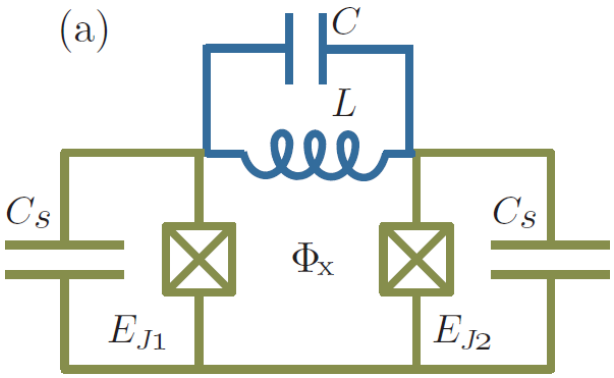

Fig. 2.1.: Circuit of a longitudinal qubit-resonator coupling (Image taken from [25])

2.2. Longitudinal qubit readout

This section addresses the difference in longitudinal qubit readout and discusses a theoretic proposal how to realize it.

2.2.1. Introduction

The circuit on which the theoretical proposal relies is quickly presented. Reference [25] discusses how to read out a qubit in the longitudinal case. They propose a layout in which a transmon qubit is longitudinally coupled to, and phase-biased by a classical resonator. Fig. 2.1 depicts a lumped-element schematic of such a circuit. The resonator (colored in blue) with frequency $\omega_\mathrm{r} = \frac{1}{\sqrt{LC}}$ is coupled to the SQUID loop (colored in green) by the two Josephson junctions of energy $E_{\mathrm{J}1}$ and $E_{\mathrm{J}2}$, which are shunted by the capacitance C_S. The junctions' capacitances will be denoted by $C_{\mathrm{q}1,2}$. This circuit will realize a longitudinal readout as demonstrated below. From now on the loop containing the two qubit Josephson junctions and the linear (or Josephson junction array) inductor will be called the SQUID loop due to its similarities to a superconducting quantum interference device (SQUID).
To continue, a brief discussion of the circuit realizing the longitudinal coupling and its Hamiltonian shall be given in subsection 2.2.2. This discussion heavily relies on the supplemental material of ref. [25]. Subsequently the longitudinal qubit readout itself is treated in subsection 2.2.3.

2.2.2. Proposed circuit realization and Hamiltonian

Now a discussion of an experimental realization of the theoretical proposal from section 2.2.1 is treated. The Hamiltonian and the coupling terms will be derived and discussed.
Reference [25] proposes to realize the circuit shown in Fig. 2.1 with a coplanar waveguide version depicted in Fig. 2.2. The dark green shaded squares indicate Josephson junctions and the dark blue square stands for a Josephson junction array. The Josephson junction array replaces the linear inductor of Fig. 2.1 to increase the coupling inductance. The

following discussion of the Hamiltonian follows the supplementary part of ref. [25].
The Lagrangian consisting of the resonator, resonator-qubit-interaction and qubit part $\mathcal{L} = \mathcal{L}_\mathrm{r} + \mathcal{L}_\mathrm{qr} + \mathcal{L}_\mathrm{q}$ of the circuit of interest depicted in Fig. 2.1 is derived by standard circuit theory [26]. The resonator part reads

$$\mathcal{L}_\mathrm{r} = \left(\frac{\Phi_0}{2\pi}\right)^2 \int_{-L}^{0-} \left(\frac{C^0}{2}\dot{\psi}^2(x,t) - \frac{1}{2L^0}(\partial_\mathrm{x}\psi(x,t))^2\right) dx + E_{\mathrm{J}r}\cos\left(\psi(0)\right) + \frac{C_{\mathrm{J}r}}{2}\dot{\psi}^2(0) \quad (2.6)$$

where $\psi(x)$ is the position-dependent field amplitude inside the resonator, L the resonator length with capacitance per unit length C^0 and inductance per unit length L^0. $C_{\mathrm{J}r}$ denotes the capacitance of the coupling Josephson junction array, $E_{\mathrm{J}r}$ its energy and $\psi(0)$ the discontinuity of the resonator wave function due to the coupling junction which finally provides the longitudinal interaction. The resonator-qubit coupling plus the qubit term of $\mathcal{L}$ is

$$\mathcal{L}_\mathrm{q} + \mathcal{L}_\mathrm{qr} = \left(\frac{\Phi_0}{2\pi}\right)^2 \left[\frac{C_{\mathrm{q}1}}{2}\dot{\phi}_1^2 + \frac{C_{\mathrm{q}2}}{2}\dot{\phi}_2^2 + \frac{C_\mathrm{S}}{2}\dot{\theta}^2\right] + E_{\mathrm{J}_1}\cos(\phi_1) + E_{\mathrm{J}_2}\cos(\phi_2) \quad (2.7)$$

where $\phi_{1,2}$ denote the phase drop over the junction 1 and 2. Using flux quantization condition around the loop allows one to define a new set of variables $\phi_1 = \delta/2 - \theta$ and $\phi_2 = \delta/2 + \theta$. This leads to

$$\begin{aligned}\mathcal{L}_\mathrm{q} + \mathcal{L}_\mathrm{qr} = \left(\frac{\Phi_0}{2\pi}\right)^2 &\left[\frac{C_{\mathrm{q}1} + C_{\mathrm{q}2}}{2}\dot{\delta}^2 + \frac{C_S + C_{\mathrm{q}1} + C_{\mathrm{q}2}}{2}\dot{\theta}^2 + (C_{\mathrm{q}2} - C_{\mathrm{q}1})\dot{\delta}\dot{\theta}\right] \\ &+ E_{\mathrm{J}_1}\cos\left(\frac{\delta}{2} - \theta\right) + E_{\mathrm{J}_2}\cos\left(\frac{\delta}{2} - \theta\right)\end{aligned} \quad (2.8)$$

with θ the phase drop across the shunt capacitance. If we assume the resonator phase-bias to be small (i.e. $\psi(0) \ll 1$), the Lagrangian becomes in zeroth-order in $\psi(0)$ after application of trigonometric addition theorems

$$\mathcal{L}_\mathrm{q} = \left(\frac{\Phi_0}{2\pi}\right)^2 \frac{C_S + C_{\mathrm{q}1} + C_{\mathrm{q}2}}{2}\dot{\theta}^2 + E_{\mathrm{J}\Sigma}\left(\cos\left(\frac{\Phi_\mathrm{x}}{2}\right)\cos(\theta) - d\cdot\sin\left(\frac{\Phi_\mathrm{x}}{2}\right)\sin(\theta)\right) \quad (2.9)$$

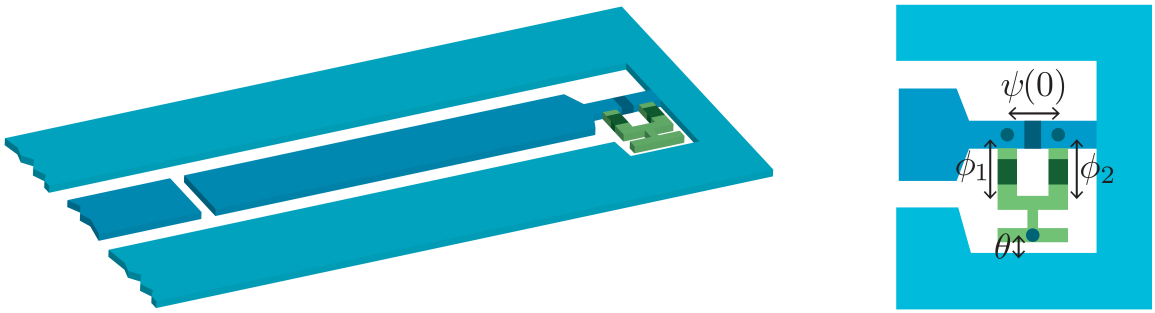

Fig. 2.2.: Coplanar waveguide realization of the circuit shown in Fig. 2.1 proposed by Didier *et al.* (Image taken from ref. [25])

with

$$E_{\mathrm{J}\Sigma} = E_{\mathrm{J}1} + E_{\mathrm{J}2} \quad \text{and} \quad d = \frac{E_{\mathrm{J}2} + E_{\mathrm{J}1}}{E_{\mathrm{J}\Sigma}} \tag{2.10}$$

where d is the junction asymmetry. Now a Legendre transformation from θ to it's conjugate charge n can be performed to obtain

$$\hat{H}_{\mathrm{q}} = 4E_{\mathrm{C}}\hat{n}^2 - E_{EJ\Sigma}\left[\cos\left(\frac{\Phi_{\mathrm{x}}}{2}\right)\cos(\hat{\theta}) - d\cdot\sin\left(\frac{\Phi_{\mathrm{x}}}{2}\right)\sin(\hat{\theta})\right] \tag{2.11}$$

with E_{C} the charging energy

$$E_{\mathrm{C}} = \frac{e^2}{2(C_S + C_{\mathrm{q}1} + C_{\mathrm{q}2})} \tag{2.12}$$

slightly modified compared to the Cooper pair box charging energy [28] since the coupling is not capacitively realized by C_g, but inductively over $\psi(0)$. Projecting Eq. (2.11) into the qubit subspace $\{|0\rangle, |1\rangle\}$ leads to

$$\hat{H} = \omega_{\mathrm{r}}a^\dagger a + K(a^\dagger a)^2 + \frac{1}{2}\omega_{\mathrm{q}}\sigma_{\mathrm{z}} + g_{\mathrm{z}}(a + a^\dagger)\hat{\sigma}_{\mathrm{z}} + g_{\mathrm{x}}(a + a^\dagger)\hat{\sigma}_{\mathrm{x}} \tag{2.13}$$

with

$$\begin{aligned} g_{\mathrm{z}} &= -\frac{E_{\mathrm{J}}}{2}\left(\frac{2E_{\mathrm{c}}}{E_{\mathrm{J}}}\right)^{\frac{1}{2}}\sqrt{\frac{\pi Z_0}{R_K}}\sin\left(\frac{\pi\Phi_{\mathrm{x}}}{\Phi_0}\right)\eta \\ g_{\mathrm{x}} &= dE_{\mathrm{J}}\left(\frac{2E_{\mathrm{c}}}{E_{\mathrm{J}}}\right)^{\frac{1}{4}}\sqrt{\frac{\pi Z_0}{R_K}}\cos\left(\frac{\pi\Phi_{\mathrm{x}}}{\Phi_0}\right)\eta \end{aligned} \tag{2.14}$$

where $Z_0 = \sqrt{\frac{L^0}{C^0}}$, $R_K = \frac{h}{e^2}$ the resistance quantum, K the Kerr non-linearity and d the Josephson energy asymmetry. The participation ratio η is defined as

$$\eta = \frac{L_{\mathrm{J}}}{L_{\mathrm{r}}} \tag{2.15}$$

with L_{J} denoting the coupling inductance and L_{r} the total inductance of the resonator modes. For the lumped element limit where the only inductance of the resonator consists of the coupling inductor, $\eta \to 1$ since $L_{\mathrm{R}} \to L_{\mathrm{J}}$. Important to note:
As ref. [29] points out in detail, for a CPWG realization L_{r} is not equal to the total inductance based on the characteristic inductance per unit length L^0 of the resonator. L_{r} strongly depends on the location of the Josephson junction inside the coplanar waveguide resonator and on the change of inductance of the resonator modes across the Josephson junction and may thus differ largely from mode to mode.
Aside from the quadratic term, the Hamiltonian of Eq. (2.13) resembles the result obtained in Eq. (2.3), but with an additional transversal coupling. The quadratic term in $(a^\dagger a)$ originates from the use of a Josephson junction array to couple the resonator to the qubit instead of a classical inductor. In experiments this is done to achieve larger inductance of the coupling inductor in smaller spacial scales compared to classical inductors realized with

relatively long meandering lines. However this quadratic term is almost negligible since $K \propto N^{-2}$ for N the number of junctions in the array. For more detailed discussion of this term see ref. [25].
Concerning the coupling terms, as already pointed out in section 2.1, the Hamiltonian exhibits transversal $g_{\mathrm{x}}(a+a^{\dagger})\hat{\sigma}_{\mathrm{x}}$ and longitudinal $g_{\mathrm{z}}(a+a^{\dagger})\hat{\sigma}_{\mathrm{z}}$ terms. However the transversal term has a factor d in front which for perfect junction symmetry vanishes as Eq. (2.10) suggests. For almost perfectly symmetric junctions the longitudinal coupling is thus dominating the qubit-resonator interaction.

Conclusion

The realization proposed by ref. [25] can produce a dominating longitudinal coupling. The longitudinal coupling can be enlarged if instead of a coplanar waveguide resonator a lumped element resonator is used.

2.2.3. Longitudinal qubit readout

Now that an experimental realization with a dominating loingitudinal coupling is proposed, the actual qubit readout is addressed.
Reference [25] derives for the longitudinal coupling a minor qubit-state dependent resonator frequency shift of

$$\pm\frac{g_{\mathrm{z}}}{\omega_{\mathrm{r}}+\frac{i\kappa}{2}} \tag{2.16}$$

with κ the cavity leakage rate. The qubit state can thus not be detected by resonator spectroscopy like the transversal coupling case. Instead they propose to modulate the coupling at the resonator frequency ω_{r}:

$$g_{\mathrm{z}}(t) = \bar{g}_{\mathrm{z}} + \tilde{g}_{\mathrm{z}}\cos(\omega_{\mathrm{r}}t) \tag{2.17}$$

This modulation causes the Hamiltonian in the interaction picture to look like

$$\hat{H} = \frac{1}{2}\tilde{g}_{\mathrm{z}}\hat{\sigma}_{\mathrm{z}}(a+a^{\dagger}) \tag{2.18}$$

which causes a large qubit-state dependent shift of the resonator frequency by $\pm\tilde{g}_{\mathrm{z}}/\kappa$. Compared to the dispersive readout, this would correspond to

$$\bar{n} = \left(\frac{g_{\mathrm{z}}}{\kappa}\right)^2 \approx 100 \tag{2.19}$$

photons for $\tilde{g}_{\mathrm{z}} \approx 10\kappa$ which is far away from the dispersive limit. The modulation of g_{z} with amplitude $\tilde{g}_{\mathrm{z}}$ is directly related to the flux modulation between Φ and $\Phi + \Delta\Phi$:

$$\tilde{g}_{\mathrm{z}} = -\frac{E_{\mathrm{J}}}{2}\left(\frac{2E_{\mathrm{c}}}{E_{\mathrm{J}}}\right)^{\frac{1}{2}}\sqrt{\frac{\pi Z_0}{R_K}}\eta\left[\sin\left(\frac{\pi\Phi_{\mathrm{x}}}{\Phi_0}\right) - \sin\left(\frac{\pi(\Phi_{\mathrm{x}}+\Delta\Phi)}{\Phi_0}\right)\right] \tag{2.20}$$

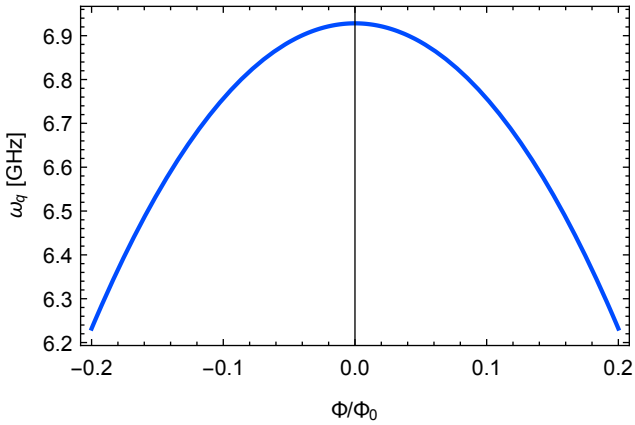

Fig. 2.3.: Flux dependent qubit frequency for $E_C = 0.3$ GHz, $E_{J\Sigma} = 20$ GHz and $d = 0.02$

since Eq. (2.14) shows that the coupling is proportional to the flux. The modulation of the flux modifies also the Josephson energy of the qubit:

$$E_J(\Phi) = E_{J\Sigma}\cos\left(\frac{\pi\Phi}{\Phi_0}\right)\sqrt{1 + d^2\tan\left(\frac{\pi\Phi}{\Phi_0}\right)} \tag{2.21}$$

and thus its frequency

$$\omega_q = \sqrt{8E_C E_J} \tag{2.22}$$

But as can be seen in Fig. 2.3 for small modulations $\Delta\Phi < 0.1\Phi_0$ around the sweet spot where $\Phi = 0$, the qubit frequency changes are minor. Furthermore the qubit frequency has no influence on the coupling between the resonator and the qubit as Eq. (2.14) shows.
The qubit state readout can be summarized as follows: If the flux Φ_x through the SQUID loop is modulated at the frequency of the resonator ω_r, the coupling between the resonator and the qubit is enabled and the resonator experiences a qubit state dependent phase shift.

2.3. Signal to noise ratio (SNR)

The different coupling mechanisms have different SNR characteristics. These are briefly compared below.
The difference of the transversal to the longitudinal coupling mechanisms manifests itself not only in the properties described in section 2.1, but also in the SNR. As derived in ref. [25, 30] the transversal signal-to-noise ratio is given by

$$\mathrm{SNR}_\chi = \sqrt{8\kappa\tau}\frac{|\epsilon|}{\kappa}\left[1 - \frac{2}{\kappa\tau}\left(1 - e^{-\frac{1}{2}\kappa t}\cos\left(\frac{\kappa\tau}{2}\right)\right)\right] \tag{2.23}$$

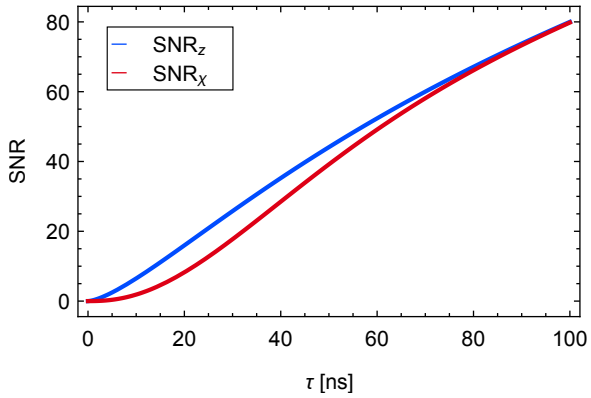

Fig. 2.4.: SNR comparison for $\tilde{g}_z = \epsilon = 175$ MHz, $\kappa/2\pi = 15$ MHz

with measurement time τ, coupling rate κ and ϵ the coherent drive amplitude. For the longitudinal coupling the SNR reads

$$\mathrm{SNR}_z = \sqrt{8\kappa\tau}\frac{|\tilde{g}_z|}{\kappa}\left[1 - \frac{2}{\kappa\tau}\left(1 - e^{-\frac{1}{2}\kappa t}\right)\right] \tag{2.24}$$

where $\tilde{g}_z$ is the modulation amplitude of the longitudinal coupling (cf. section 2.2.3).
The longitudinal coupling and the resulting SNR_z has a few advantages over the SNR_χ. The first one is shown in Fig. 2.4 where for short measurement times τ the SNR_z increases faster than the SNR_χ. Analytically this originates from the $\cos\left(\frac{\kappa\tau}{2}\right)$ factor in the SNR_χ which is a less efficient pointer state trajectory for a state measurement. The second advantage is that the SNR can be exponentially improved by a single-mode squeezing of the input state on the resonator. For the full derivation of SNR_z and details about the pointer state separation look at ref. [25] and its supplemental materials.
It can be concluded that the longitudinal SNR_z has an advantage over the transversal SNR_χ for short measurement times and therefore can be utilized for fast and accurate qubit state readout.

2.4. Resonance circle fit for notch type geometries

All the experiments described in the present thesis were performed in a so called "notch type geometry", schematically depicted in Fig. 2.5. In the notch type geometry a resonator is probed in reflection, but the the chip on which the resonator is embedded as a whole is measured in transmission. The crucial advantage of a transmission measurement is the option of determining the internal quality factor in case of a small resonator coupling capacitance.
Reference [31] offers a detailed discussion of how to robustly and efficiently fit a circle to complex scattering data. This fitting method was applied to every complex scattering data fit performed in this thesis. Below a brief overview of the fitting method is given.
According to the paper from Probst *et al.* a general model for the complex scattering

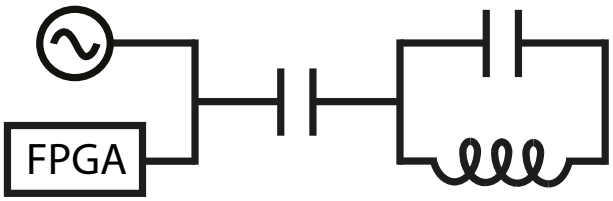

Fig. 2.5.: Schematic circuit of a notch type experiment.

coefficients is given by

$$S_{21}^{\text{notch}}(f) = ae^{i\alpha}e^{-2\pi f\tau}\left[1 - \frac{(Q_\text{l}/|Q_\text{c}|)e^{i\phi}}{1 + 2iQ_\text{l}(f/f_\text{r} - 1)}\right] \tag{2.25}$$

where the prefactor takes the environment into account and the rest the ideal resonator in dependence of the probing frequency f. The resonance frequency is denoted by f_r, the loaded quality factor by Q_l and the coupling capacitor by Q_c. The environment is described by the impedance mismatch ϕ, the phase shift α and the electric length τ. The environment may come along with an additional amplitude a. First the environment is treated by removing the optical length which rotates the resonance circle in its canonical position. In a second step a rough circle is fitted to the complex scattering data. Afterwards the distance of the circle fit to the origin is used to translate the circle to the origin. Then the angle between the real axis and the circle aperture is determined and the data is rotated in the complex plane. After this procedure a phase versus frequency fit is performed with the fit function

$$\theta(f) = \theta_0 + 2\text{arctan}\left(2Q_\text{l}\left[1 - \frac{f}{f_\text{r}}\right]\right) \tag{2.26}$$

which yields the loaded quality factor Q_l, the resonance frequency f_r and the offset phase θ_0. The offset phase $\theta_0 = \beta - \pi$ where β is the rotation angle of the complex circle with respect to the real axis. From this fit all the parameters of the complex circle are known and the remaining parameters can be reconstructed.

3.Sample design and fabrication

3.1. Determination of circuit parameters

How the circuit parameters were extracted from the realization proposal shown in Fig. 2.2 is described in this section.
In a first step, the circuit of the realization proposal shown in Fig. 2.2 was modeled in Microwave Office, a circuit analyzer program. The circuit is displayed in Fig. 3.1 and shows a lumped element (LE) realization of the resonator instead of a coplanar waveguide (CPWG) version. The two Josephson junctions forming the qubit degree of freedom were modeled as LC-resonators.
The circuit parameters for the simulation were chosen such that the resonator frequency was approximately at 4.5 GHz and the qubit frequency at 7 GHz since the output line of the cryostat has a tunable parametric amplifier between 4 and 8 GHz. The qubit resonance

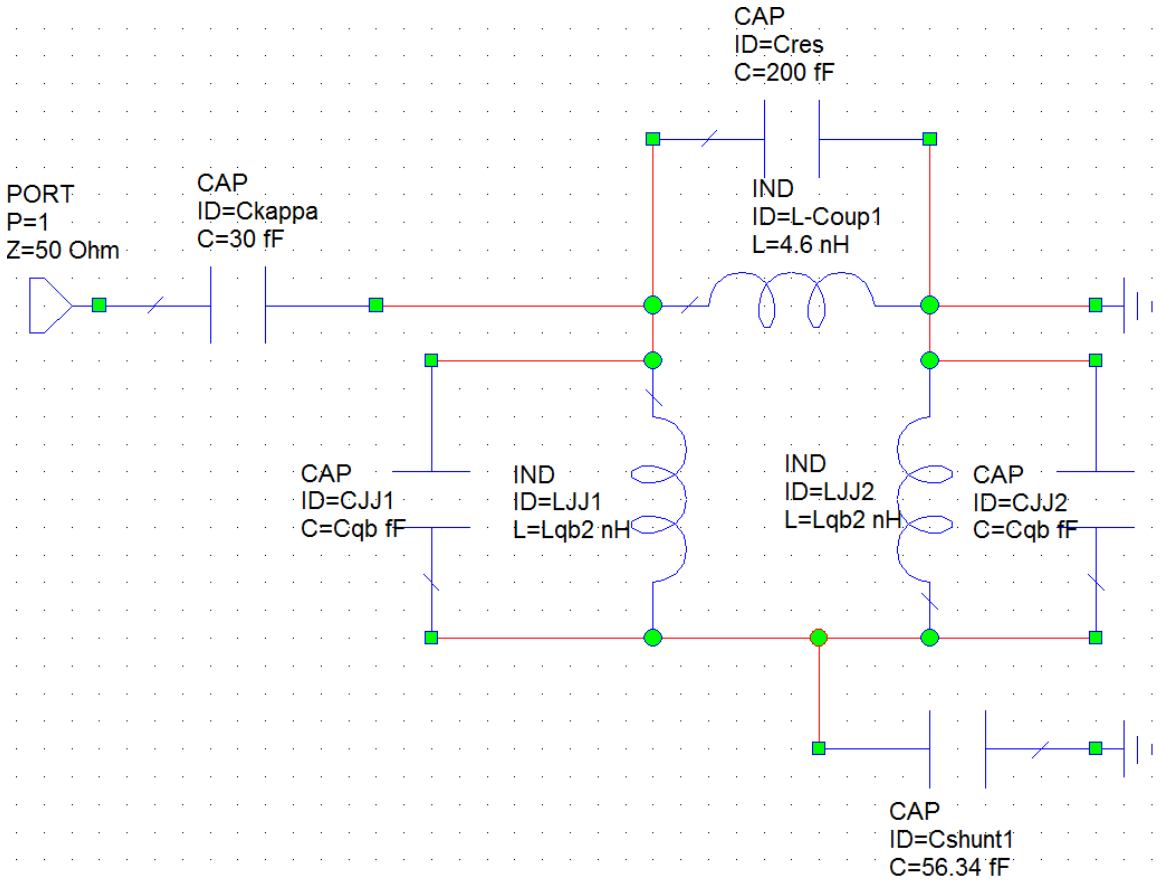

Fig. 3.1.: Cuircuit schematic of the lumped element realization modeled in Microwave Office from NI AWR design environment® version 11.0r. $Ckappa$ is the coupling capacitor, $Cres, L\text{-}Coup1$ capacitance and inductance of the resonator, $CJJ1 = 6$ fF, $LJJ1 = 16.3$ nH capacitance and inductance of the first (second) Josephson junction and $Cshunt$ the shunt capacitance to ground.

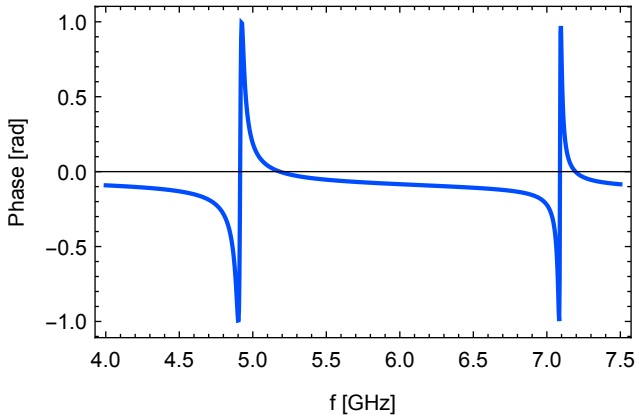

Fig. 3.2.: Simulated Arg[s_{21}] of the LE version. The resonator resonance lies at 4.91 GHz and the qubit frequency at 7.09 GHz

frequency was adopted from the proposal in ref. [25] with $E_C \approx 0.3$ GHz and $E_{J\Sigma} \approx 20$ GHz. The coupling capacitance C_κ and thus the coupling rate κ was set such that the proposed relation of $g_z \approx 10\kappa$ was fulfilled. Fig. 3.2 shows the simulation result for the parameters as shown in Fig. 3.1. The resonator resonance lies at 4.91 GHz and the qubit frequency at 7.09 GHz.

The decision to realize the resonator in a LE version was based on the comparison of the different SNRs and thus the quibt-resonator coupling strengths. For an optimal SNR of the qubit-state readout, a large longitudinal coupling g_z of the qubit to the resonator is required (cf. eq 2.24). The longitudinal coupling strength g_z however depends for given qubit properties E_C, E_J linearly on the participation ratio η (cf. eq 2.14). Thus an η close to 1 is preferable. If the participation ratio η_{LE} for the lumped element version is assumed to be ca. 1 and η_{CPWG} is adopted from ref. [25] to be ca. 0.53, the longitudinal coupling g_z for the LE version is almost two times larger than for the CPWG version. For this reason it was decided to realize the lumped element version.

The circuit parameter extraction yielded that the resonator capacitances need to be between 100 fF and 250 fF and the Josephson junction inductance ca. 4.5 nH to produce a resonance in the observable frequency range. Furthermore the qubit frequency with $E_C \approx 0.3$ GHz and $E_{J\Sigma} \approx 20$ GHz lies in the frequency window as well.

3.2. Translation of the circuit to a physical sample geometry

The process which leads from the circuit schematic with known parameters to the sample design is shown below. Furthermore different considerations and constraints which influenced the sample design are discussed in detail.

Figure 3.3 shows a rendered image of a sample realizing the lumped element circuit depicted in Fig. 3.1. The resonator is colored in red, the island in blue, the SQUID loop with the white Josephson junctions in orange, the flux-line in pale blue, the ground in gray, the charge-line in pale red and the transmission line in green. The flux-line and the charge-line

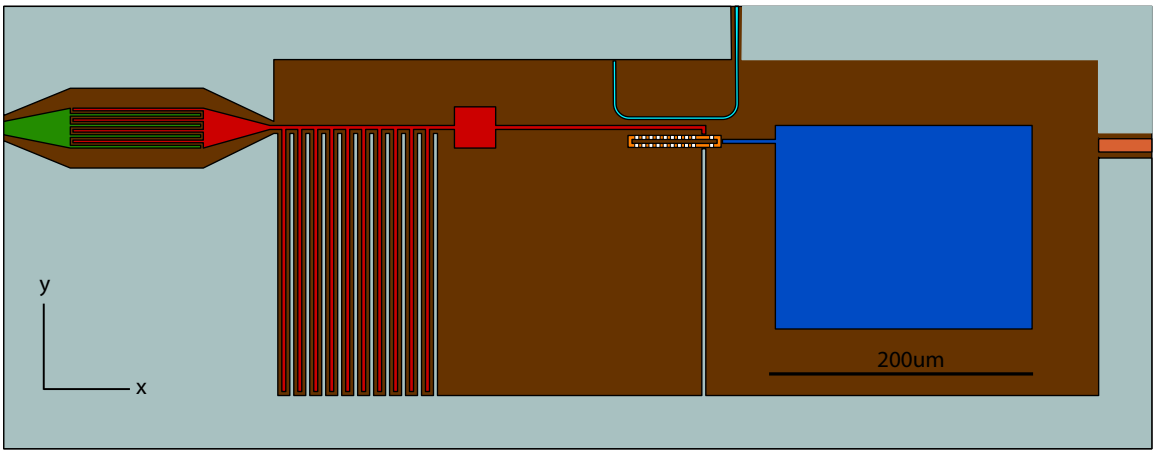

Fig. 3.3.: Design for the grounded version

were not modeled in the Microwave Office model since they couple weakly to the rest of the structure. The red square on the resonator is for the connection of the layer deposited in the photo lithography step to layers evaporated by the electron beam lithography step. The aforementioned elements of the sample design (resonator, island, ...) are discussed in the paragraphs below including the reasons and simulations results from Ansoft Maxwell® V14.0 leading to the final element shape and location.

Coupling capacitor

The coupling capacitor to the transmission (green) to the resonator (red) line was realized as a standard finger capacitor with a finger length of 100 μm and thickness of 2 μm in order to reduce overall capacitor size.

Resonator capacitor

The resonator capacitance was chosen to have standard finger length of 200 μm and thickness of 3 μm. For ca. 200 fF the width of such a finger capacitor is ca. 120 μm.

Charge-line

The charge-line was impedance matched to 50 Ω and exhibits a capacitive coupling of ca. 1 fF to the island. The small capacitive coupling reduces qubit decay into the charge-line and therefore increases the coherence time.

SQUID loop

The SQUID loop size and shape is the result of a minimization of the area to reduce flux noise and a maximization of the number of Josephson junctions to reduce the nonlinearity. The SQUID loop is a rectangle of ca. 4μm $\times$ 50 μm size with a total of 18 Josephson junctions. The rectangular shape is due to the Josephson junction deposition process which allows deposition either in x or y direction on the sample.A closeup of Fig. 3.3 around the

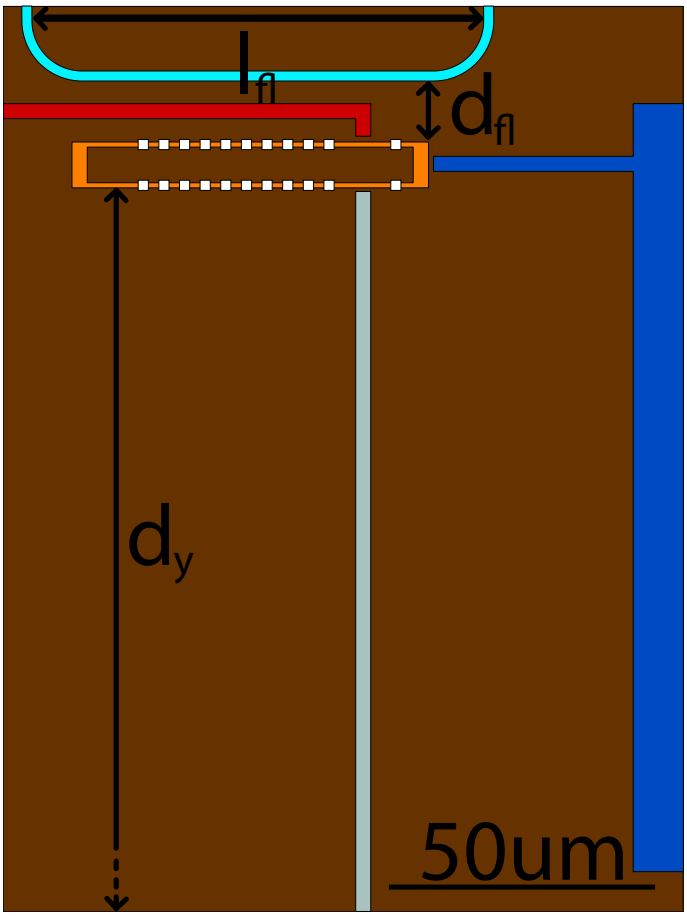

Fig. 3.4.: Closeup of SQUID loop, resonator-island connection and flux-line

SQUID loop is shown in Fig. 3.4.
The SQUID loop is located at a maximum distance d_y to the lower edge of the ground plane. This position minimizes the capacitive coupling of the resonator and the distance d_{fl} to the flux line.

Flux-line

The parallel flux line length denoted as l_{fl} in Fig. 3.4 was optimized to ca. 90 μm for a 4μm×50 μm SQUIDloop size with simulations and analytical calculations. The termination of the fluxline to ground was chosen to minimize the length of the fluxline and to increase the standing wave frequencies.

Island

The island size exhibits a size of 193μm × 153 μm and symmetric distance to ground of 50 μm. The aforementioned parameters lead to a simulated renormalized qubit charging energy $E_{C\Sigma}$ of 0.3 GHz. The island-ground distance was not increased above 50 μm due to

ref. [32] and the island size was realized as a large pad due to the results of ref. [33].

3.3. Introduction of the floating version

The quality of the sample can be improved by choosing an appropriate sample design. These considerations lead to a second, slightly modified design which is described below.
The sample fabrication process consists of two different steps. In a first step the niobium is deposited on a sapphire wafer with photo lithography and in a second step smaller structures made out of aluminum, such as Josephson junctions, are added with an electron beam lithography step. At points where a galvanic connection between the niobium and aluminum occur, oxide layers of unknown properties may form on the surface and thus increase the resistance of the galvanic connection. The increased resistance damps qubit excitations and reduces its coherence time.
To avoid these resistive interfaces a design with a floating ground was introduced as shown in Fig. 3.5. The fabrication of the floating version includes the deposition of the ground plane (grey), the transmission line (green), the charge line (pale red) and the flux line (pale blue) withing the photo lithography step and the deposition of the resonator (red), teh SQUID loop with Josephson junctions (orange), the island (blue) and the floating ground (yellow) in the electron beam lithography step.

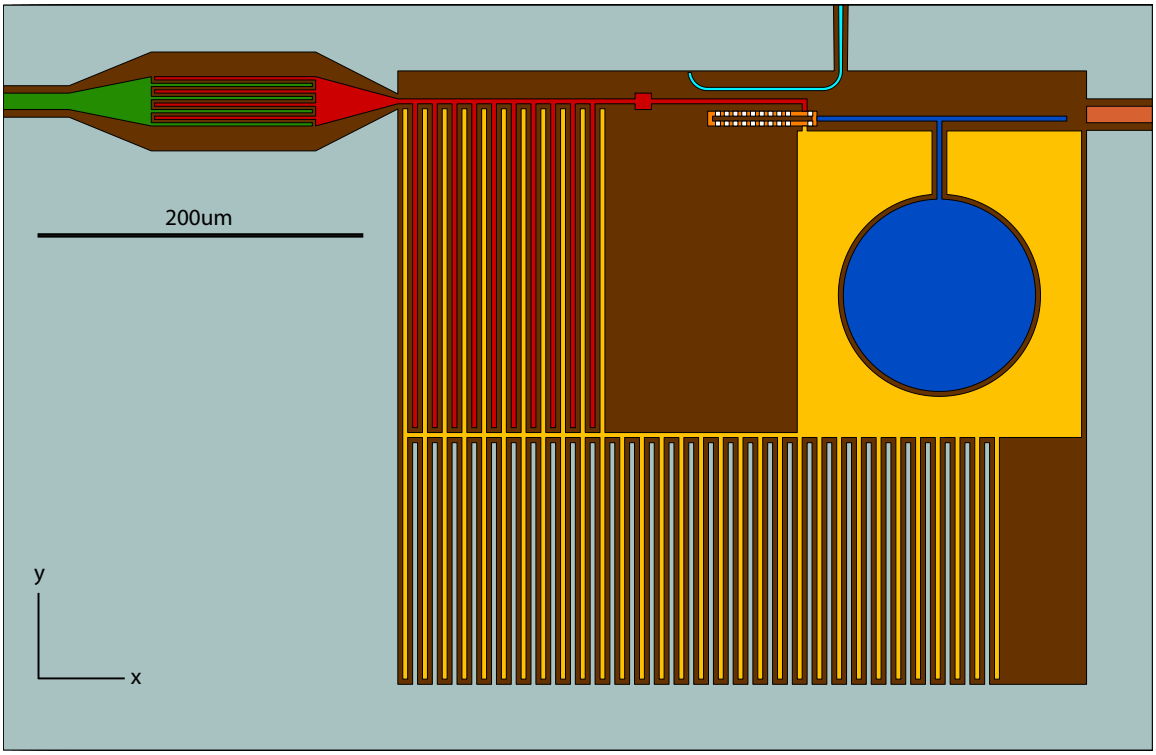

Fig. 3.5.: Ansoft Maxwell simulation design for the floating version. The floating ground to ground capacitor is not distributed over the whole length due to the fact that the island finger design was discarded after the mask creation.

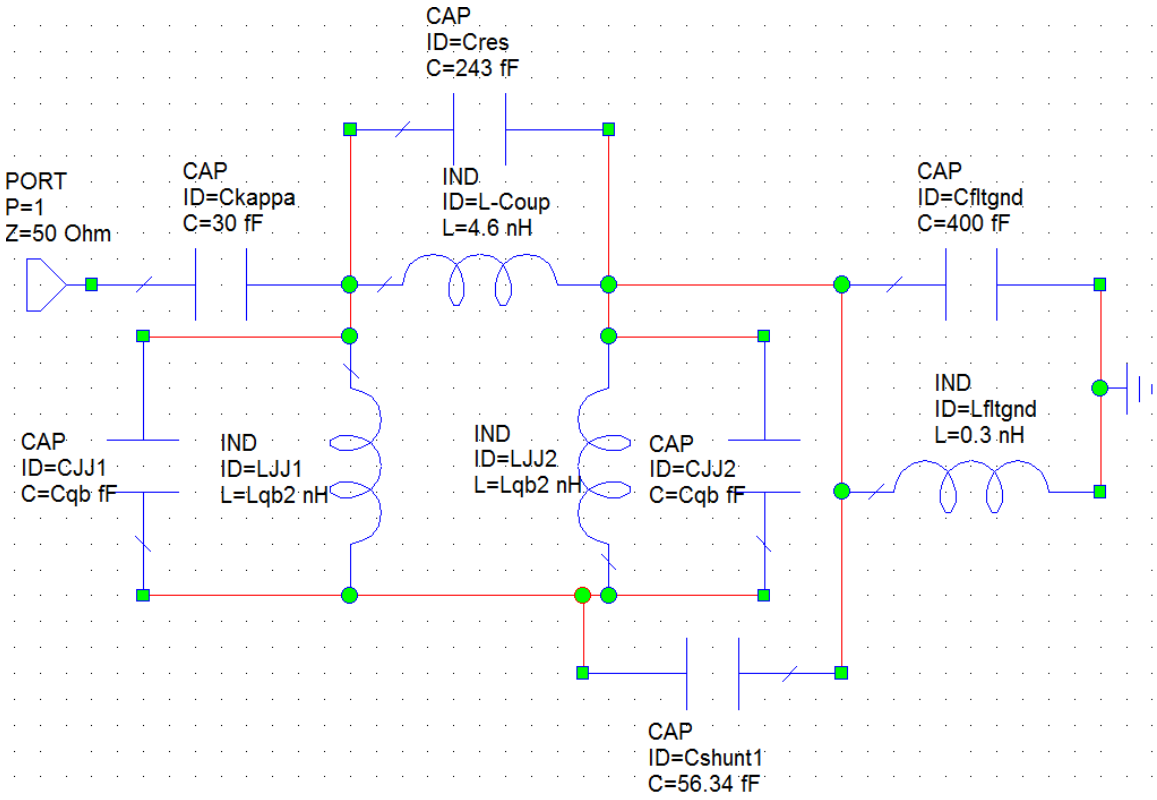

Fig. 3.6.: Cuircuit schematic of the floating version. The capacitances and inductances are as in Fig. 3.1 except the the large capacitance $Cfltgnd$ of the floating ground to the real ground. The $fltgnd$ inductance accounts for the additional inductance of the floating ground structure.

The circuit schematic of the floating version is shown in Fig. 3.6. A comparison with Fig. 3.1 reveals that the only difference consists in the additional capacitance to gound in the floating version. The circuit schematic accounts for the additional inductance of the floating ground. The results of the simulations show negligible differences in the resonance frequencies of less than 1.5% as Fig. 3.7 points out in comparison with Fig. 3.2.

3.4. Peculiarities of the floating version

Island design

The island shape and size of the floating version was determined by the minimization of the spurious capacitive coupling to the other structures, the maximization of the island size (cf. ref. [33]) and the avoidance of edges (cf. ref. [34]) under the constraints of the qubit charging energy amounting to ca. 0.3 GHz and the capacitive coupling of the island-charge line being ≤ 1 fF. The island radius is 58.5 μm and the distance to the charge line 12 μm as depicted in Fig. 3.8.

Floating ground

Maxwell simulations performed for the floating version showed capacitances of the floating

ground to ground $C_{\text{fltgnd}-\text{gnd}} > 1900$ fF.

Capacitance of resonator to floating ground and resonance frequency

The introduction of a floating ground modifies the estimation of the resonance frequency. Although spurious capacitances renormalize the resonances frequency in the grounded version, in the floating version the spurious capacitance of the resonator to direct ground $C_{\text{res}-\text{gnd}}$ is the major contribution to the renormalization. A schematic of the situation is shown in Fig. 3.9. The total equivalent capacitance of the structure is given by

$$C_{\text{tot}} = \frac{C_{\text{res}-\text{fltgnd}} \cdot C_{\text{fltgnd}-\text{gnd}}}{C_{\text{res}-\text{fltgnd}} + C_{\text{fltgnd}-\text{gnd}}} + C_{\text{res}-\text{gnd}} \tag{3.1}$$

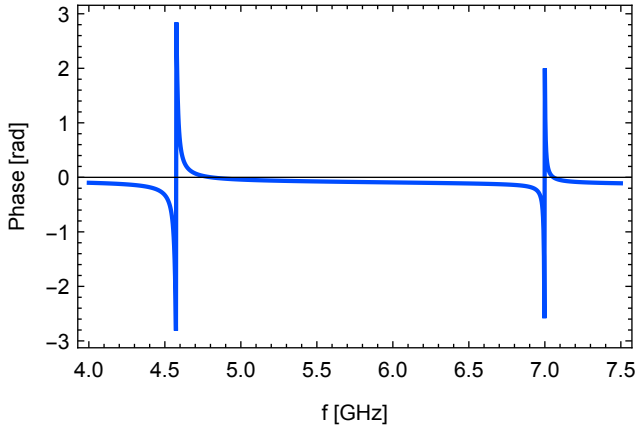

Fig. 3.7.: Simulated frequency dependence of the phase of the floating version. The resonator resonance is at 4.58 GHz and the qubit at 7.0 GHz.

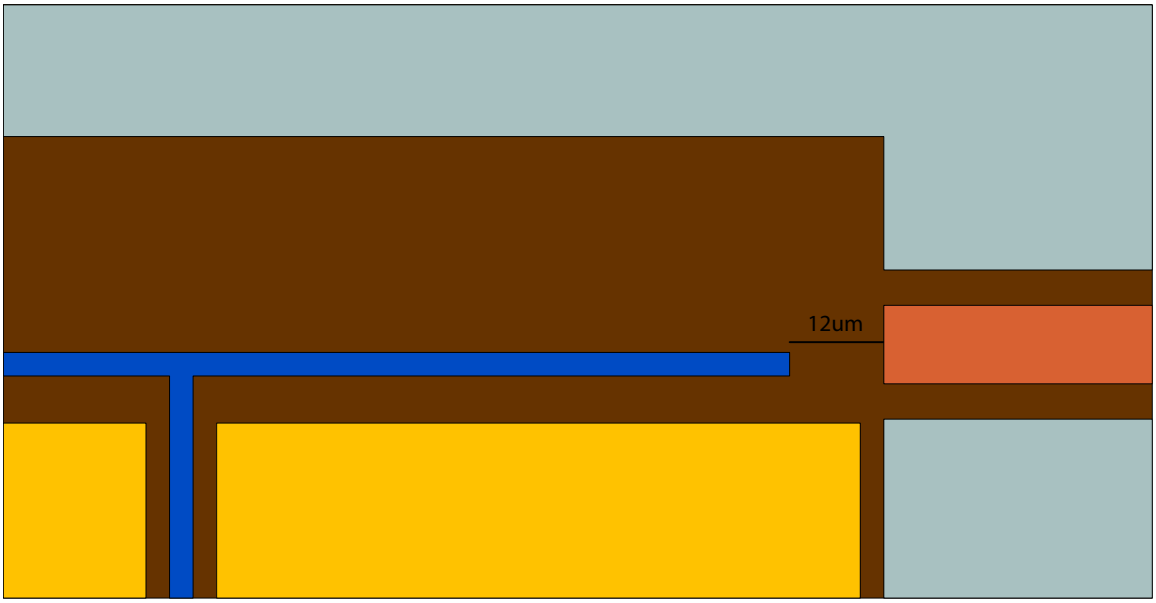

Fig. 3.8.: Distance of 12 μm of the bomb handle (blue) to the charge-line (light red). Grey is the enclosing ground plane and yellow the floating ground (cf. Fig. 3.5)

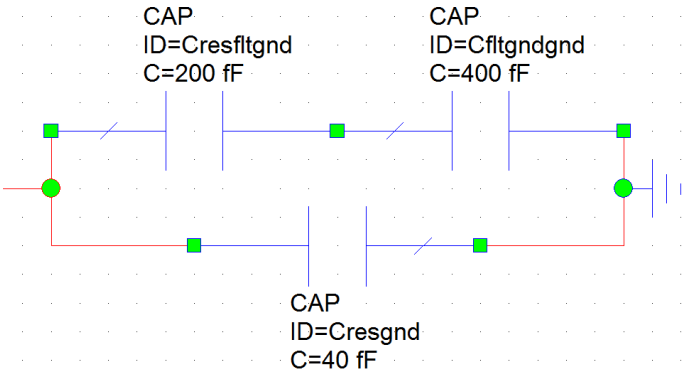

Fig. 3.9.: Circuit schematic of the spurious capacitance $C_{\mathrm{res-gnd}}$ in the floating version

which for $C_{\mathrm{fltgnd-gnd}} \gg C_{\mathrm{res-fltgnd}}$ is

$$C_{\mathrm{tot}} \approx C_{\mathrm{res-fltgnd}} + C_{\mathrm{res-gnd}} \tag{3.2}$$

Since this condition is satisfied for $C_{\mathrm{fltgnd-gnd}} > 19000$ fF and $C_{\mathrm{res-fltgnd}} \approx 200$ fF, the resonance frequency estimation has to be based on Eq. (3.2). This is the reason why the resonator capacitances in Fig. 3.1 and Fig. 3.6 differ by 40 fF and still exhibt the same resonance frequencies.

3.5. Sample Fabrication

For the samples for measurement rounds 1 to 3 a different wafer was used than for sample 4. The first wafer was created by niobium deposition on a sapphire wafer with photolithography. For the second wafer aluminum instead of niobium was used. On both wafers size 1 chips with 7×2mm size were written.
In a second step the rest of the structures were added with electron beam lithography. Large structures such as island pads or finger capacitors were written with a different write field than small structures such as Josephson junctions. However, every structure deposited by electron beam lithography consists of two layers with a thin insulating layer in between. This originates from the fact that the same deposition process as for Josephson junctions is applied and for Josephson junctions the two layers with the insulating sheet in between is desired. All structures written by electron beam lithography are double-layered. But the capacitance between the two layers is so large that it can be considered connected and the Josephson inductances decreases with interface size.
It should be noted, that a new Josephson junction fabrication recipe had to be developed in order to create Josephson junctions of different scales at the same time. This work was done by Simone Gasparinetti and represents a milestone for the longitudinal coupling to be realizable.

4.Experimental Setup

This section describes the experimental setup of the four performed measurement rounds. The cabeling configuration accessing the chip inside the cryostat are shown.
All experiments were performed in a BlueFors cryogen-free dilution refrigerator system®. In a nutshell, five shields at different temperature stages, where the outermost serves as a vacuum can, protect the sample against thermal radiation. Inside the cryostat two layers of $\mu-$metal shields provide protection against magnetic fields. The sample chip is mounted on a PCB (printed circuit board) which itself is enclosed in a sample holder of oxygen-free copper.

4.1. Measurement rounds 1 and 2

Fig. 4.1 depicts the experimental setup of the first measurement round. The colored dashed horizontal lines represent the different temperature shields and stages inside the cryostat. The chip is indicated by the grey dashed box. The radio frequency(RF) signal of the measurement passes a direct current(DC) block and is attenuated three times by -20 dB. Afterwards the signal enters the sample chip. After the chip, the signal passes two circulators and is filtered by a bandpass filter of $4 - 10$ GHz and amplified by a high electron mobility transistor (HEMT) at the 4K stage. At room temperature the signal passes a DC-block and is further amplified before it is analog downconverted to intermediate frequency by mixture with the local oscillator (LO). After a subsequent digital down conversion the signal is recorded by a field programmable gate array (FPGA). The FPGA memory is finally read out by the measurement computer (PC).
The dashed box schematically depicts the configuration of resonators which were placed on the sample chips for the first two measurement rounds.

4.2. Measurement round 3

The experimental setup of measurement round 3 is shown in Fig. 4.2. In addition to the setup shown in Fig. 4.1, the setup for measurement round 3 includes a coil to apply external magnetic field and a second input line for a second chip. The output signals of the chip are routed on the same circulator and then connected to the output line. The advantage of this setup is to use the same output line for both chips. The disadvantage is that the output of one chip is attenuated by 20 dB.

4.3. Measurement round 4

The experimental setup of measurement round 4 is shown in Fig. 4.3. The experimental setup of measurement round 4 includes one measurement line labeled with RF and for each of the two resonators on the sample chip a flux (FL) and a charge line (CL). This setup

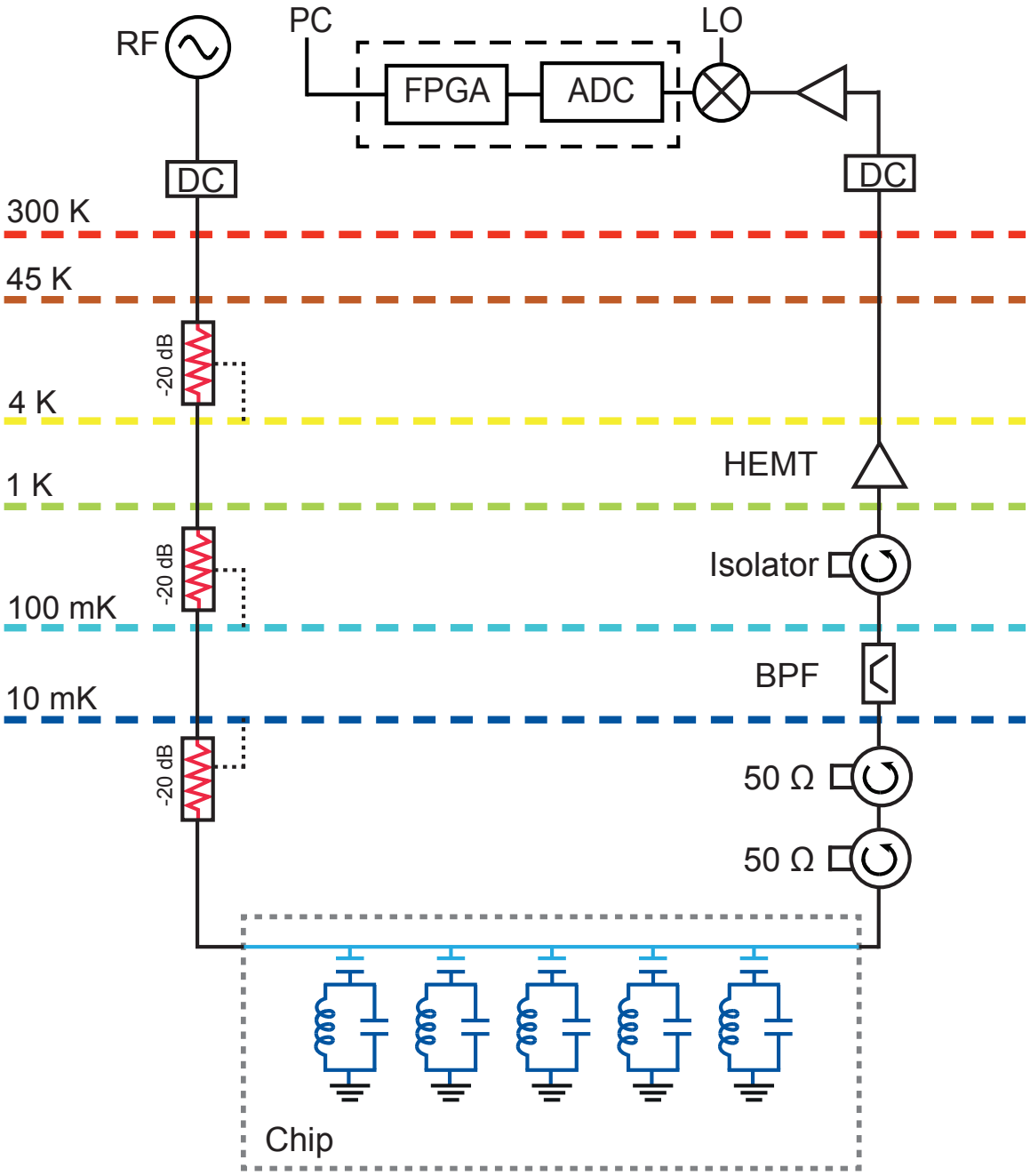

Fig. 4.1.: Schematic of experimental setup of measurement round 1 and 2. The temperature stages are indicated by the colored dashed lines and the thermalization of the attenuators by dotted lines. RF stands for radio frequency, DC for the direct current block and PC for the measurement computer.

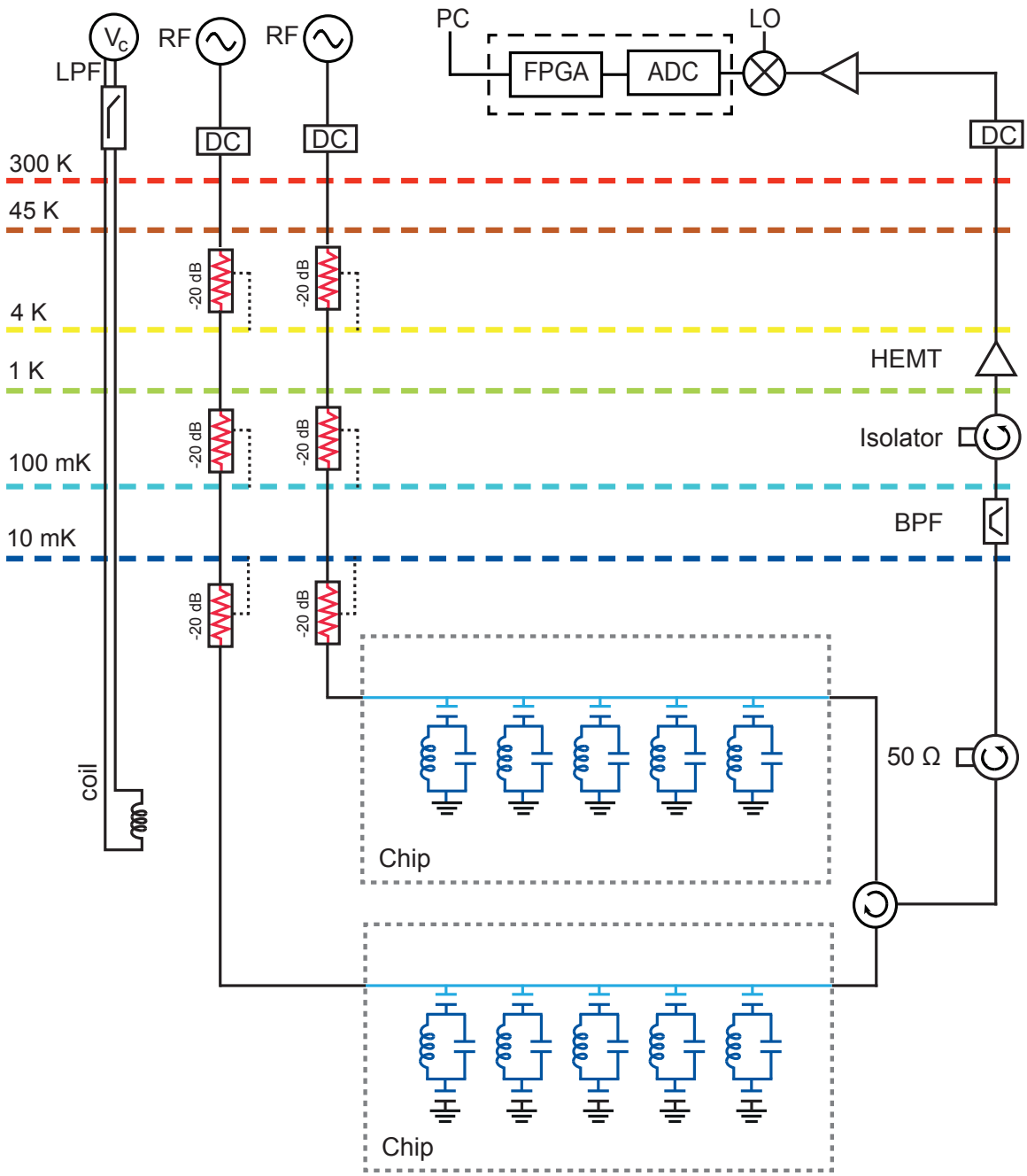

Fig. 4.2.: Schematic of experimental setup of measurement round 3. Both chips, indicated by the grey dashed boxes, are mounted in the same sample holder on the same PCB but can be separately addressed with RF signals and are readout via the same output line. The temperature stages are indicated by the colored dashed lines and the thermalization of the attenuators by dotted lines. RF stands for radio frequency, DC for the direct current block and PC for the measurement computer.

allows to measure both resonators on the chip with just one input and one output line. However an individual measurement of the two resonators is not possible.

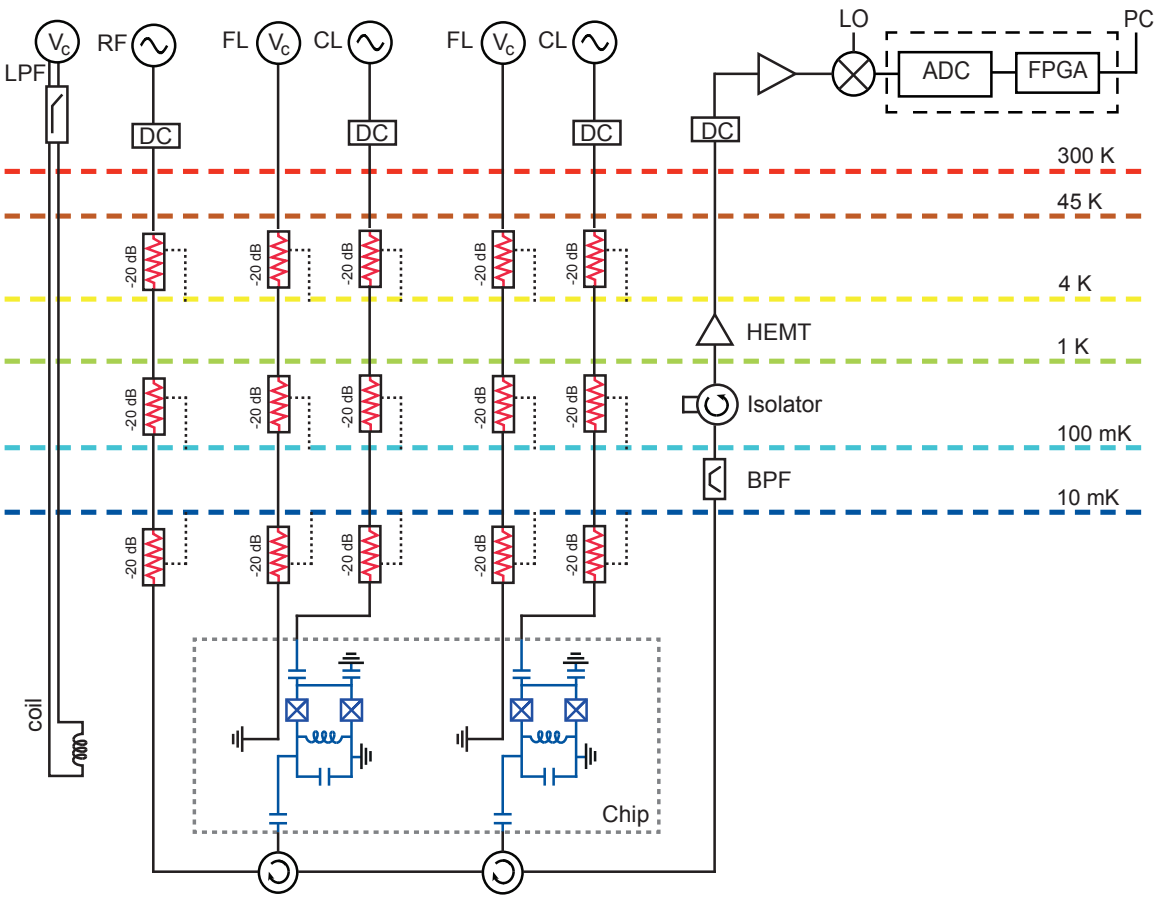

Fig. 4.3.: Schematic of experimental setup of measurement round 4. The temperature stages are indicated by the colored dashed lines and the thermalization of the attenuators by black dotted lines. RF stands for radio frequency, DC for the direct current block and PC for the measurement computer. CL is the charge line and FL the flux line which is grounded on the chip (grey dashed box).

5.Results and Discussion

5.1. Measurement rounds 1 and 2

This section briefly discusses samples 1 and 2, the important outcomes of the first two measurement rounds and insights for the sample fabrication.
Samples 1 and 2 consist of a 2×7 mm chip with 5 resonators arranged in a notch type geometry (cf. Fig. 4.1, section 2.4). The only difference is the coupling rate of the resonators to the transmission line which was designed to be ca. 40 KHz for sample 1 and ca. 1 MHz for sample 2.
The optical image examination of sample 1 showed that all structures deposited by electron beam lithography were 1.2 μm thicker in $x-$direction than designed. This effect originates from the fact that during the electron beam lithography two layers of aluminum are deposited with two different angles of $\pm 45^o$. This causes the structures to be larger in one dimension by twice the thickness of the deposited layer which is ca. 600 nm. The fabrication of the sample 2 included the correction for this effect.
The RF measurement of sample 1 and 2 during the first two measurement rounds did however not show the designed resonances although indications for a working measurement setup were given such as the power transition depending on the HEMT power or the characteristics of the $4 - 10$ GHz bandbass filter. Therefore a detailed discussion and documentation of the samples, the measurement results and the conclusions can be found in section A.1 and A.2 of the appendix. The possible reasons for the failure are discussed there as well.
Although measurement round 1 and 2 failed, the double layer effect when writing finger capacitors and other structures with electron beam lithography was illuminated and corrected for in the subsequent designs.

5.2. Measurement round 3

The design and predicted characteristics of sample 3a and 3b for the third measurement round are discussed below. The results of the optical image examination after the fabrication are given together with the measurement results. This section closes by a discussion of the results and a subsequent conclusion.

5.2.1. Samples for measurement round 3

Purpose

For the third measurement round two sample versions were prepared, a floating (sample 3a) and a grounded (sample 3b). On both samples two inductors were realized with a meandering line and others with a SQUID array or a Josephson junction array. The aim

was to investigate whether the fabrication process is yielding functioning Josephson junctions. The meander inductor would serve as a confirmation for a functioning readout setup. The SQUID introduces a tunablity of the resonance frequency which facilitates its unique identification from spurious resonances.

Description of floating version design (sample 3a)

The resonators are arranged as shown in fig.5.1. They are capacitively coupled in a notch type geometry to the transmission line (green). Table 5.1 presents an overview of the capacitors and inductor types of the different resonators on sample 3a which are numerated from left to right. None of the resonators contained the Josephson junctions for the qubit. Except for resonator 3, the island was removed in resonator 1 and 4 for spatial reasons and in 2 and 5 to possibly detect a difference compared to resonator 3.
The meander inductor was designed according to Stojanovic *et al.* [35] to exhibit a total inductance of 4.12 nH. The Josephson junction array and the SQUID array for resonator 2, 3 and 5 were designed by Simone Gasparinetti and expected to exhibit a total inductance of $4 - 5$ nH.
For the floating version, the coupling of the resonators to the transmission line was increased to ca. 10 MHz compared to ca. $0.1 - 1.3$ MHz for the resonators on sample 2. The floating version coupling capacitors were realized by a finger capacitor designed for ca. 23 fF with 4 fingers as depicted in Fig. 5.2. Table 5.2 shows an overview of the simulated resonance frequencies and coupling rates κ of the resonators placed on sample chip 3a. The simulation was performed with Sonnet high frequency electromagnetic software version 14.52®. The

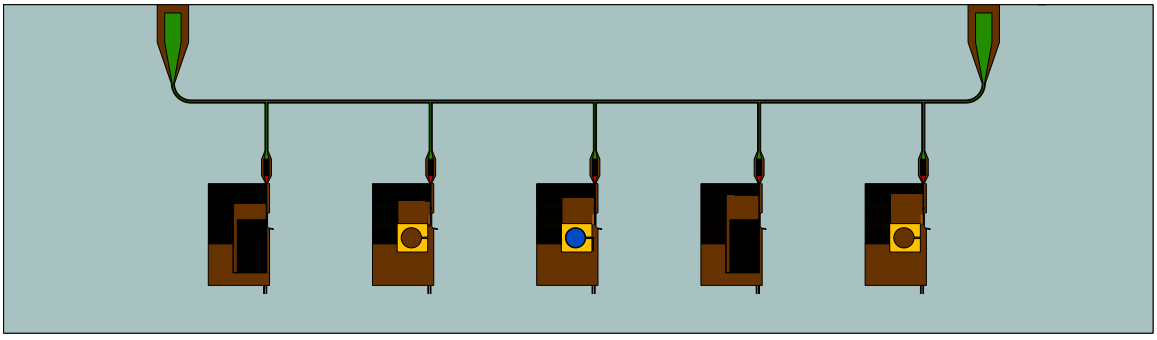

Fig. 5.1.: Schematic of sample 3a. The five resonators (cf. Fig. **??**) are capacitively coupled to the transmission line (green) in a notch type geometry. The resonators are numerated from left to right. Resonator 1 and 4 have a meander inductor, resonator 2 and 5 a Josephson junction array inductor and resonator 3 a SQUID array inductor.

Resonator	#fingers	Inductor type	Island
1	21	meander	No
2	17.1	Junction array	No
3	21	SQUID array	Yes
4	11.7	meander	No
5	10	Junction array	No

Table 5.1.: Resonator overview of sample 3a.

Resonator	Inductor type	f_r [GHz]	$\kappa/2\pi$ [MHz]
1	meander	5.382	3.7
2	Junction array	5.203	4.4
3	SQUID array	4.663	5.7
4	meander	6.473	7.4
5	Junction array	5.956	8.5

Table 5.2.: Overview of resonator resonance frequencies f_r and coupling rates κ of the 5 resonators implemented on sample chip 3a. Resonator 3 is tunable due to the SQUID array inductor and the table thus displays the aimed sweet spot values.

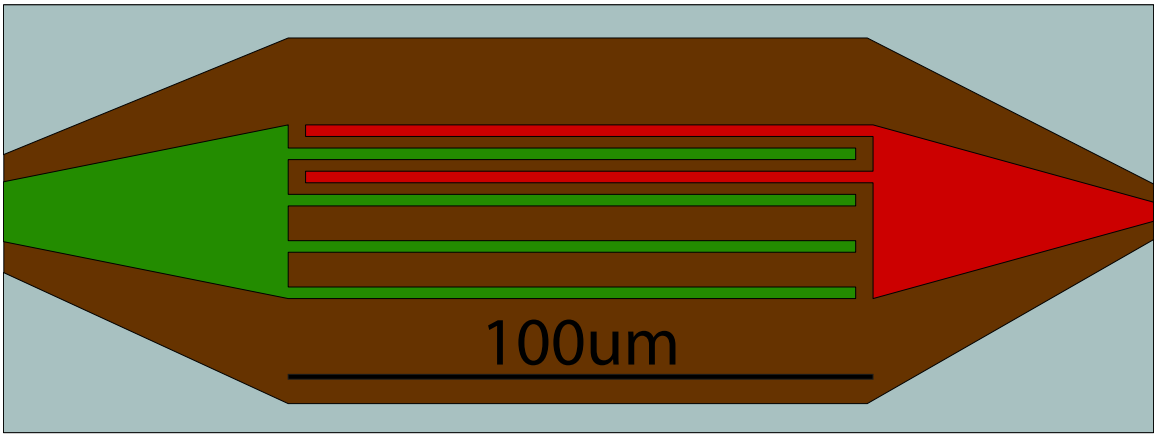

Fig. 5.2.: Rendered closeup of the coupling capacitor for sample chip 3a with 4 fingers corresponding to a capacitance of ca. 23 fF.

geometry was set up in a notch type as proposed by ref. [31]. The coupling rates κ were extracted with a complex Lorentzian fit of the simulated response. A screen shot of the Sonnet geometry is shown in Fig. B.1 in the appendix together an extended table of the simulation results.

Description of grounded version design (sample 3b)

A schematic of the grounded version sample (sample 3b) is depicted in Fig. 5.3. The resonators are arranged in the same manner as for sample 3a. Table 5.3 shows an overview of the capacitances and inductor types of the 5 resonators on chip 3b. Similar to sample

Resonator	#fingers	Inductor type
1	21	meander
2	17.1	meander
3	14.1	SQUID array
4	11.7	SQUID array
5	10	SQUID array

Table 5.3.: Overview of the grounded version of sample 3 with finger number and inductor type.

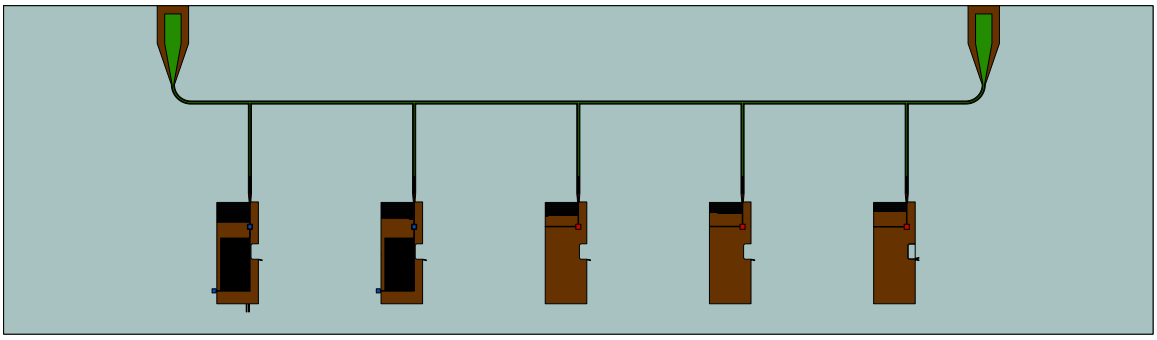

Fig. 5.3.: Schematic of sample 3b. Resonator 1 and 2 (from left to right) have a meander inductor and resonator 3 to 5 a SQUID array inductor. The resonators are capacitively coupled to the transmission line (green) in a notch type geometry.

3a, sample 3b contains 2 meander inductors and three SQUID array inductors for the resonators. The SQUID arrays were designed identical to the SQUID array on the floating version by Simone Gasparinetti. The meander inductor is identical to the one on sample 3a and exhibits an inductance of 4.12 nH. The resonance frequency of the resonators is varied with the number of capacitor fingers. Table 5.4 shows an overview of the simulated coupling rates κ and the resonance frequencies. Detailed simulation results are shown in section B.2 in the appendix.

Res.	Inductor type	f_r [GHz]	$\kappa/2\pi$ [MHz]
1	meander	5.474	4.8
2	meander	5.899	6.6
3	SQUID array	5.543	8.1
4	Junction array	5.969	10.6
5	Junction array	6.318	13.3

Table 5.4.: Overview of finger number, inductor type, simulated resonance frequency f_r and coupling rate κ_M of sample 3b.

5.2.2. Sample examination after fabrication

The dose for the electron beam lithography for samples 3a and 3b was slightly increased. The sample is cleaner, but slightly overexposed which causes the capacitor fingers to be 600 nm larger than designed, which can be observed in Fig. 5.4 by comparing the fingers written with electron beam lithography to the ones written in the photo lithography step. The Josephson Junction array is again misaligned by an angle of ca. 3^o with respect to the other structures written in the electron beam lithography step which is due to the different writing window sizes used in the deposition process. No shorts or other type of further defects were observed.
On sample chip 3b the overexposure affects only the Josephson Junctions since the capacitors were written in the photo-lithography step.
To sum up, sample 3a is cleaner than samples 1 and 2 but exhibits a slight overexposure

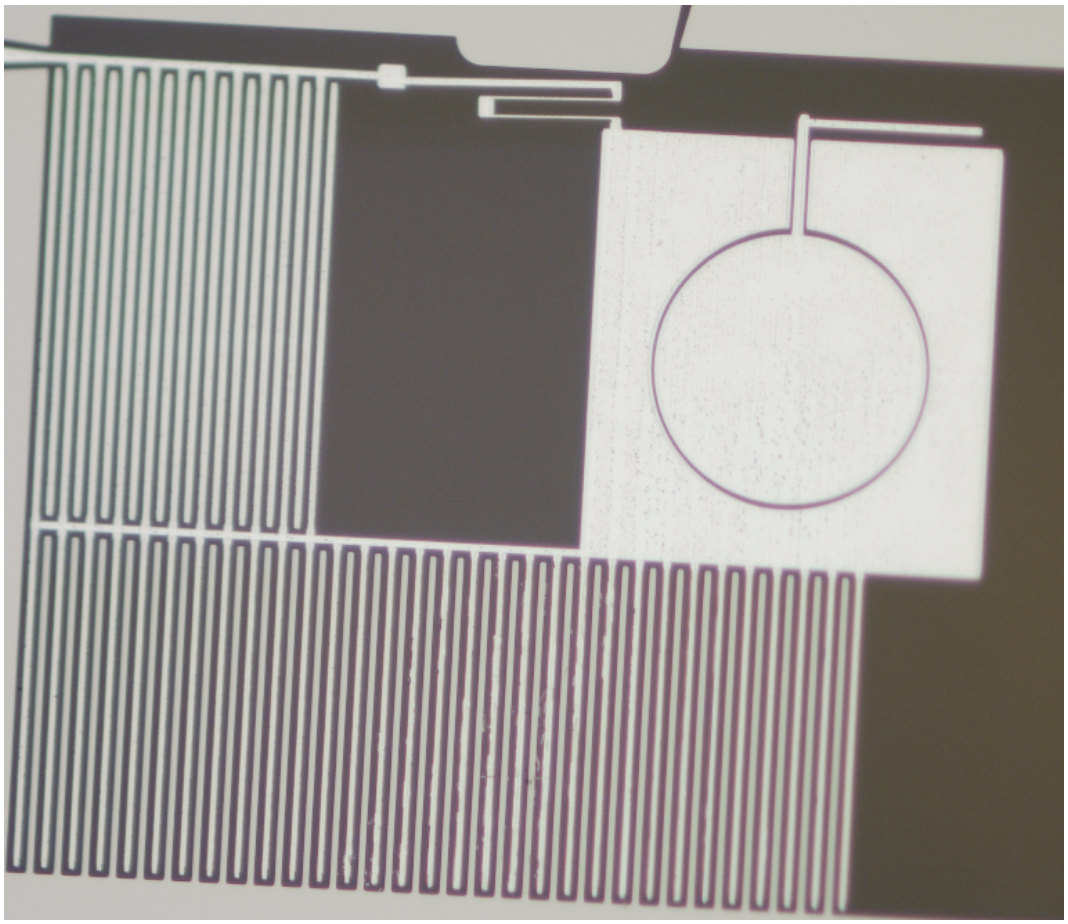

Fig. 5.4.: Optical image of resonator 1 of the floating version of sample 3.

and a misalignment of the Josephson junction array with respect to the rest of the chip.

5.2.3. Measurement results for sample 3a (floating version)

A vector analyzer network (VNA) measurement of sample 3a showed 5 distinct resonances. All resonances are well expressed in both quadratures. Figures 5.5 and 5.6 show as an example the phase data of the resonances of the second and third resonator of sample 3a for -117 dBm sample power. The meander inductor resonators (first and fourth) are more clearly expressed (cf. Fig. B.3 in the appendix). Table 5.5 shows an overview of the fit parameters of the observed resonances on the sample 3a. All values are extracted with a notch type model fit (cf. section 2.4) to the data measured with approx. -117 dBm power at the sample and no magnetic field applied. The resonator with the Josephson junction array and the resonance frequency at 5.079 GHz showed strong power dependence so that the resonance disappeared in the noise for powers > -75 dBm at the sample. The proximity to the meander inductor resonance at 5.103 GHz contributed to the reduced visibility of this resonance too. The power dependence of the other four resonances is shown in Fig. 5.7. This figure shows that the linear meander inductors show no power dependence over 5

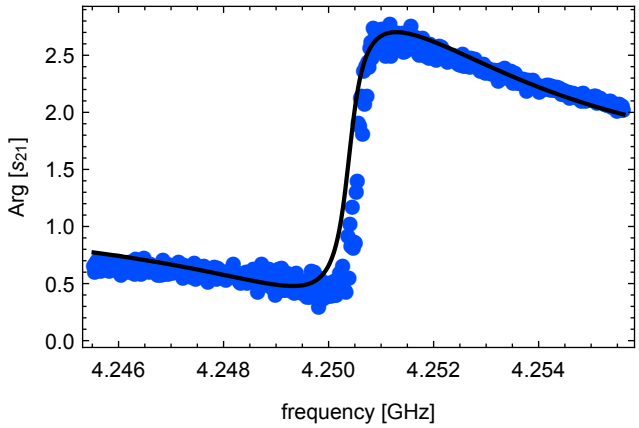

Fig. 5.5.: Phase data and fit of the second resonator on sample 3a with a Josephson junction array inductor. The data was taken for $B = 0$ V and -117 dBm sample power.

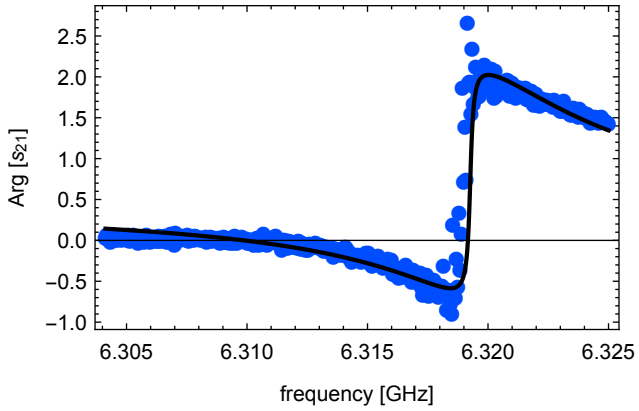

Fig. 5.6.: Phase data and fit of the third resonator on the sample 3a with a SQUID array inductor. The data was taken for $B = 0$ V and -117 dBm sample power.

Resonator	Inductor type	f_{res} [GHz]	Q_{L}	$\kappa/2\pi$ [MHz]
1	meander	5.103	722	7.1
2	Junction array	4.251	611	7.0
3	SQUID array	6.319	567	11.1
4	meander	6.132	396	15.5
5	Junction array	5.079	848	6.0

Table 5.5.: Fit parameter overview of the resonances from the sample 3a at $B = 0$ V and ca. -117 dBm sample power.

orders of magnitude whereas the non-linear inductors show a frequency red-shift.
Figures 5.8 and 5.9 show the dependence of the internal Q_{int} and external quality factor Q_{ext} on the sample power. While the external quality factor is not power dependent, the internal quality factor of the resonators with a Josephson junction array or SQUID array inductor decreases with increasing power. This behavior is in contrast to the the resonators with the meander inductors where the quality factor increases. Concerning the external quality factors of the resonators with the Josephson junction or SQUID array inductors,

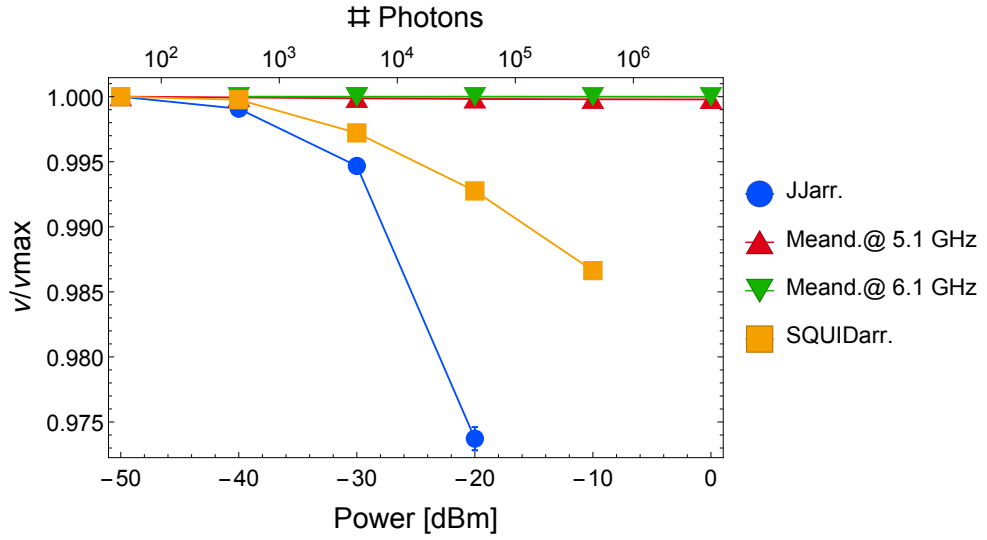

Fig. 5.7.: Power dependence of the resonance frequencies on sample 3a. Plotted is the resonance frequency at a specific VNA output power ν divided by the maximal resonance frequency ν_{max}. "JJarr." labels the resonator with the Josephson junction array, "Meand." the resonators with meander inductors and "SQUIDarr." the resonator with the SQUID array inductor.

the fits become unreliable due to increased non-linear effects with increasing power.
Except for the resonator with the SQUID array inductor, the resonance frequency and the quality factor are not expected to change with applied magnetic field. This is indeed the case (cf. figures 5.10b and B.4 in the appendix). Finally, Fig. 5.10a shows the resonance frequency dependence of the resonator with the SQUID array inductor. This dependence coincides with the tunability of the Josephson energy [6] as the fitted black line indicates. For $\phi/\Phi_0 > 1$ the deviation to the fit increases.
The obtained result follows the expectation.

5.2.4. Discussion of the floating version results (sample 3a)

A comparison of the predicted and measured frequencies and κ is shown in table 5.6. The simulated values for the coupling rate κ are simulated with Sonnet. Table 5.6 reveals that the prediction of the resonance frequencies for resonators 1 and 4 are ca. 300 MHz too low. This deviation matches the expected difference due to the thicker fingers and corresponds to an increased effective resonator capacitance of ca. 20 fF. Resonators 2 and 5 with the Josephson Junction array exhibit a ca. 900 MHz lower resonance frequency which partly is explained by the thicker capacitor finger and partly by an increased Josephson junction inductance due to the increased oxidation time in the fabrication process. Taking the 20 fF increased capacitance into account, the inductance of the Josephson junction array was simulated to be 5.8 nH. The increased inductance is consistent with the longer oxidation between fabrication and cooldown. The deviation of the resonator with the SQUID array stems from the fact that total inductance of the SQUID array was designed roughly to be ca. 4 nH. The extracted inductance from the fit shown in Fig. 5.10a is 2.8 nH. If the

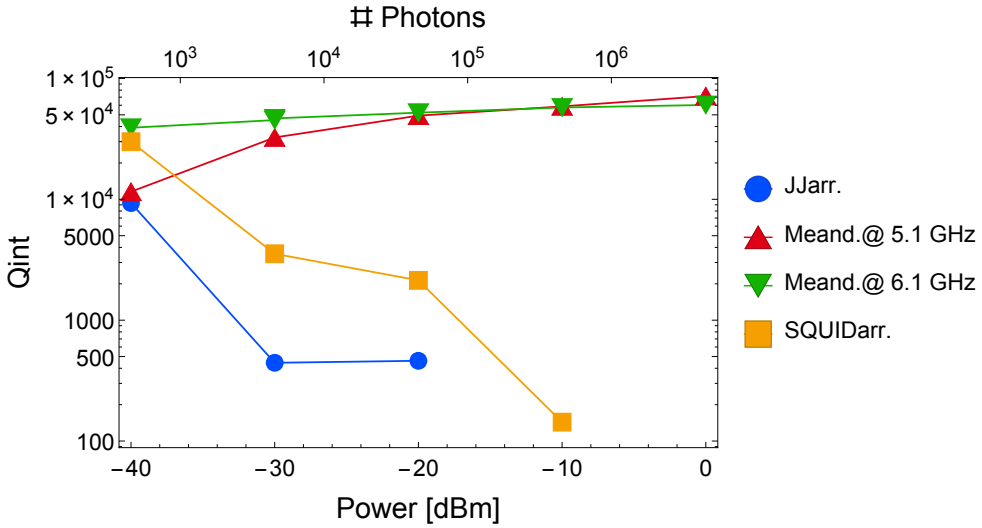

Fig. 5.8.: Power dependence of the internal quality factor Q_{int} of the resonators on sample 3a. "JJarr." labels the resonator with the Josephson junction array, "Meand." the resonators with meander inductors and "SQUIDarr." the resonator with the SQUID array inductor.

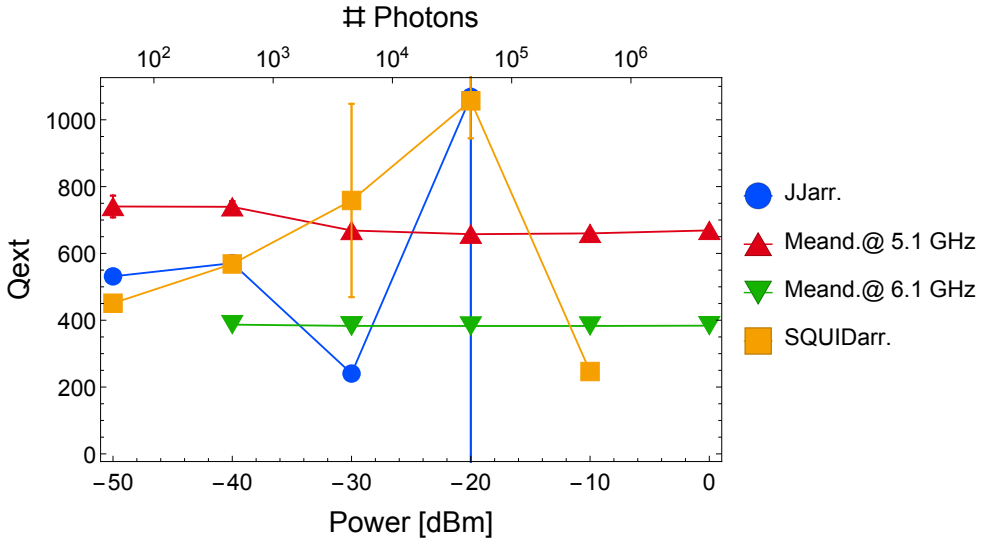

Fig. 5.9.: Power dependence of the external quality factor Q_{ext} of the resonators on sample 3a. "JJarr." labels the resonator with the Josephson junction array, "Meand." the resonators with meander inductors and "SQUIDarr." the resonator with the SQUID array inductor.

additional 20 fF are taken into account, the SQUID array inductance is 2.6 nH.
The differences in κ can partly be explained by the deviation in frequency. More investigation would be needed to evaluate why the Sonnet simulation tends to underestimate and the Microwave Office simulation to overestimate the coupling (cf. table B.1 in the appendix). For the purpose of the present thesis, the coupling accuracy however is not crucial and therefore no further study was conducted.
In a nutshell, the dependence of the resonance frequencies as a function of power or magnetic field is as expected for all resonators on the sample 3a. No inexplicable results were

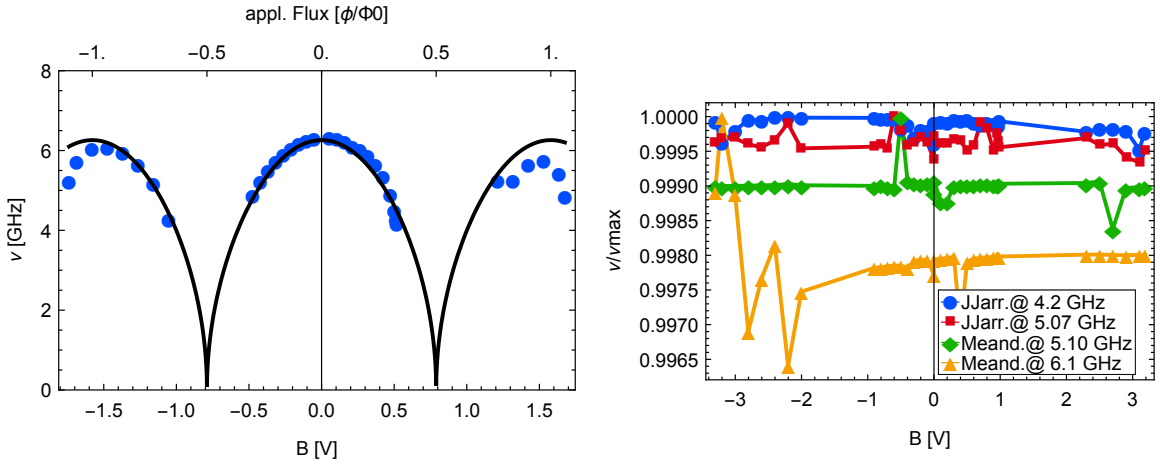

(a) Resonance frequency of the third resonator on sample 3a as a function of applied magnetic field. The black line is the fit to $1/(2\pi\sqrt{LC})\sqrt{|\cos[\pi(\phi-\phi_{\text{off}})/\Phi_0]|}$. Since the inductor consists of a SQUID array the resonance frequency is tunable with magnetic flux.

(b) Bfield dependence of the resonance frequencies on sample 3a

Fig. 5.10.: Magnetic field dependence of the resonance frequencies of sample 3a

Res.	Ind. type	f_{p} [GHz]	f_{m} [GHz]	$\lvert\Delta f\rvert$ [MHz]	$\frac{\kappa_{\text{p}}}{2\pi}$ [MHz]	$\frac{\kappa_{\text{m}}}{2\pi}$ [MHz]	$\frac{\Delta\kappa}{2\pi}$ [MHz]
1	meand.	5.382	5.103	279	3.7	7.4	3.7
2	JJ arr.	5.203	4.256	947	4.4	7.2	2.8
3	SQUID arr.	4.663	6.322	1659	5.7	16.9	11.2
4	meand.	6.473	6.136	337	7.4	14.8	7.5
5	JJ arr.	5.956	5.079	877	8.5	6.0	2.5

Table 5.6.: Comparison of prediction $(f_{\text{p}}, \kappa_{\text{p}})$ and measurement $(f_{\text{m}}, \kappa_{\text{m}})$ of the resonators on the sample 3a of the third cooldown. The deviations from the measurement to the prediction is denoted as Δf for the resonance frequency and as $\Delta\kappa$ for the coupling.

found although some quantitative deviations were measured. For the realization of a longitudinal coupling the circuit parameters have to be in the right order of magnitude which was the case.

5.2.5. Results of the grounded version

Table 5.7 shows an overview of the fit parameters of the visible resonances at zero magnetic field and -117 dBm power at the sample 3b. The resonators with the SQUID arrays were not visible at zero magnetic field and are thus not shown in table 5.7. The resonances of the resonators with the linear meander inductor were well expressed and showed comparable behavior for power and magnetic field dependence as the resonators with the meander inductor on the sample 3a. The only difference consists in a significantly smaller internal quality factor for resonators with meander inductors compared to the floating version as

Resonator	Inductor type	f_{res} [GHz]	Q_{L}	$\kappa/2\pi$ [MHz]
1	meander	5.402	1356	4.0
2	meander	5.822	1701	3.4

Table 5.7.: Fit parameter overview of the resonances from sample 3b at $B = 0$ V and -117 dBm sample power.

shown in Fig. 5.8. While Q_{int} is between 40'000 and 60'000 for the floating version, the internal quality factor Q_{int} is ca. 5'000 for the grounded version. The measurement value for the resonator at -10 dBm was omitted because the fit failed due to low data quality. The extracted internal quality factor as a function of different applied powers is shown in Fig. 5.11 for sample 3b.
The three resonators with the SQUID array inductors exhibited a lower than expected inductances, but could be tuned into the visible range between 4 and 8 GHz by applying a static magnetic field. The result is shown in Fig. 5.12.
Concluding it can be stated that the grounded version results are consistent with the results from the floating version as well as the expectations from theory and the extracted parameters are reliable.

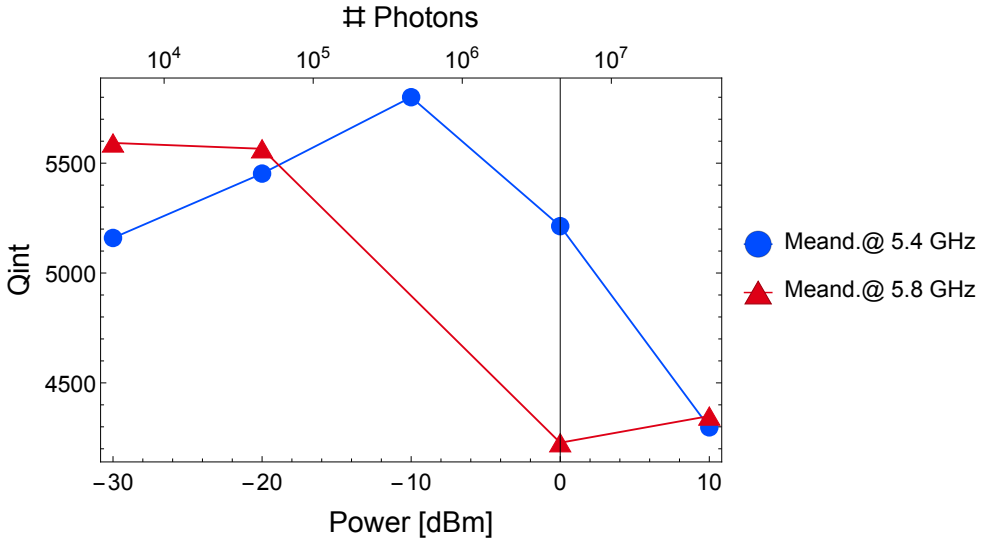

Fig. 5.11.: Fitted internal quality factors for the two resonators with the meander inductors at different sample powers for the grounded version 3b.

Res.	Ind. type	f_{p} [GHz]	f_{m} [GHz]	$\lvert\Delta f\rvert$ [MHz]	$\frac{\kappa_{\mathrm{p}}}{2\pi}$ [MHz]	$\frac{\kappa_{\mathrm{m}}}{2\pi}$ [MHz]	$\frac{\Delta\kappa}{2\pi}$ [MHz]
1	meander	5.474	5.402	72	1.8	3.4	1.5
2	meander	5.899	5.822	77	2.7	3.3	0.6

Table 5.8.: Comparison of prediction $(f_{\mathrm{p}}, \kappa_{\mathrm{p}})$ and measurement $(f_{\mathrm{m}}, \kappa_{\mathrm{m}})$ of the resonators on sample chip 3b

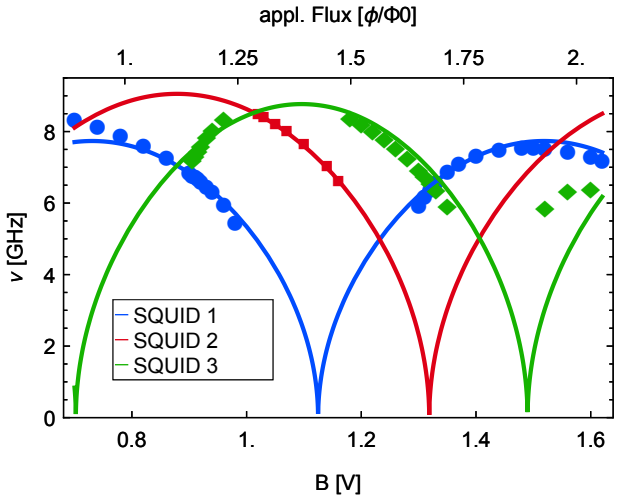

Fig. 5.12.: Resonance frequencies of the three resonators with the SQUID array inductors on sample chip 3b as a function of applied magnetic field. The full lines are the fits to $1/(2\pi\sqrt{LC})\sqrt{|\cos[\pi(\phi-\phi_{\text{off}})/\Phi_0]|}$ which describes the tunability of the SQUID array inductance as a function of magnetic flux [6].

5.2.6. Discussion of the grounded version results (sample 3b)

The prediction and the measurement values for the resonance frequencies and the coupling rate κ is shown in table 5.8. The prediction of the resonance frequency exhibits a consistent difference of +70 MHz which can be explained by an underestimation of the inductance of the meander inductor. In contrast to sample 3a, the resonance frequency prediction was more accurate due to the absence of the overexposure since the finger capacitor of sample 3b was written with photo lithography.
As for sample 3a, κ was again underestimated with the Sonnet simulation displayed in table 5.8, but overestimated with the Microwave Office simulation (cf. table B.2)
The extracted maximal inductance of the resonators with the SQUID array from the fit shown in Fig. 5.12 yielded 2.4 nH for resonator 3, 2.1 nH for resonator 4 and 2.5 nH for resonator 5. These results coincide with the identical SQUID array from the sample 3a.
For the results of sample 3b the same conclusion can be drawn as for the floating version results. The dependence of the resonance frequencies as a function of power or magnetic field is as expected for all resonators and no inexplicable results were found although 70 MHz deviation for the frequency and ca.1 MHz deviation for the coupling rates were measured. For the realization of a longitudinal coupling the circuit parameters have to be in the right order of magnitude which was the case.

5.2.7. Conclusion for measurement round 3

The measurement results for the floating and the grounded version are consistent. The capacitances do coincide and if the additional finger thickness due to the overexposure is taken into account, the results agree better. This observation also holds for the SQUID arrays

on sample 3a and 3b. The parameters of the lumped element resonators with Josephson junction inductors were extracted, as well as, their behavior as a function of magnetic field and measurement power characterized. They exhibit lower quality factors than lumped element resonators with meander inductors. Further experiments have to show whether this will adversely affect a qubit measurement.
Although all the lumped element resonators with Josephson junction array inductors worked, their reliability and inductance accuracy is poor, since measurement round 3 was the first round showing functioning Josephson junction arrays.
Therefore it can be concluded, that the sample design is suitable for a microwave frequency experiment and that Josephson junction arrays can be implemented as inductors for lumped element resonators. However, these resonator exhibit lower performance and reliability than resonators with meander inductors.

5.3. Measurement round 4

This section delivers a description of the sample designed for measurement round 4 and its purposes. Furthermore it is compared to the previous samples. The findings of an optical image examination after fabrication are given afterwards. Furthermore the deduction from a performed resistance measurement is discussed. The section is closed by a discussion of the results of measurement round 4 which are provided with a focus on the resonator tunability. Finally the question of the presence of longitudinal coupling is addressed and a theoretical explanation is given.

5.3.1. Sample for measurement round 4

Purpose

After the successful test of the lumped element resonators with Josephson Junction arrays in measurement round 3 (cf. section 5.2), a test of the sample as a whole with a qubit was fabricated. Therefore the two Josephson junction connecting the island with the Josephson junction array were added with the electron beam lithography. Recently, before measurement round 4 was started, experiments with qubits were conducted by QUDEV group members where aluminum instead of niobium is used for the photo lithography step. The T1 times they extracted where the highest measured up to then. Therefore it was decided to fabricate sample 4 also completely out of aluminum. The grounded version was chosen since the galvanic connection of unknown property between the niobium and the aluminum was no longer a problem.

Description of sample

A rendered image of the resonator arrangement on the chip is shown in Fig. 5.13. Two resonators with different capacitors, but otherwise identical properties are placed at the two ends of the chip, rotated by 180^o with respect to each other. The capacitances of the finger

Fig. 5.13.: Rendered image of sample 4.

capacitors are 144 fF/14 fingers (left) and 119 fF/11.7 fingers (right). The right qubit island (blue) is accessed by a charge-line from below (pale red) and the SQUID loop (orange) can be tuned through a flux-line accessing from above which is closely terminated to ground. The capacitors and coupling rates κ are identical to those of resonator 3 (left) and 4 (right) of sample 3b. A closeup of the left side of the chip is depicted in figure 5.14. The white boxes on the squid loop symbolize the Josephson junctions. The Josephson junction array was designed to be identical to the last cooldowns with an inductance of 5.8 nH.
The pale green parts are deposited in the same electron beam lithography step as the blue island. The large green extension in $x-$direction in the bottom right corner of the sample is because the $\pm 45^o$ deposition angle of the electron beam is in the $x-$direction and will thus not make a proper connection over the edge in $y-$direction of the sapphire substrate (brown) and the aluminum (grey). The thick bar allows for a possible earlier connection in $y-$direction, which reduces the additional inductance from the longer distance to ground.
The coupling of the resonator (red) to the transmission line (green) is the same as for measurement round 3.
Sample 4 has two resonators with a qubit coupled to them addressable with a flux and a charge line.

5.3.2. Sample examination after fabrication

The optical image of the left side of sample 4 is shown in Fig. 5.15. The photo shows scratches on the aluminum layer deposited in the electron beam lithography step on the island and the connection part of the SQUID loop to the ground in the lower right corner. This damage stems from a resistance measurement of the junctions yielding 3.32 kΩ. Since the Josephson array is identical to the one used for measurement round 3 with 5.8 nH and this resistance measurement measured one qubit junction in series with the array and these two in parallel with the other qubit junction, the resistance of a single qubit junction can be calculated to be 5.1 kΩ. This corresponds to an inductance of 5.9 nH. The junction inductance is so low due to a Junction size correction in the wrong direction. Originally an inductance of 16.3 nH was planned. Figure 5.16 shows a closeup of Fig. 5.15 around the SQUID loop and the flux-line. Fig. 3.4 depicts the location of the Josephson junctions.

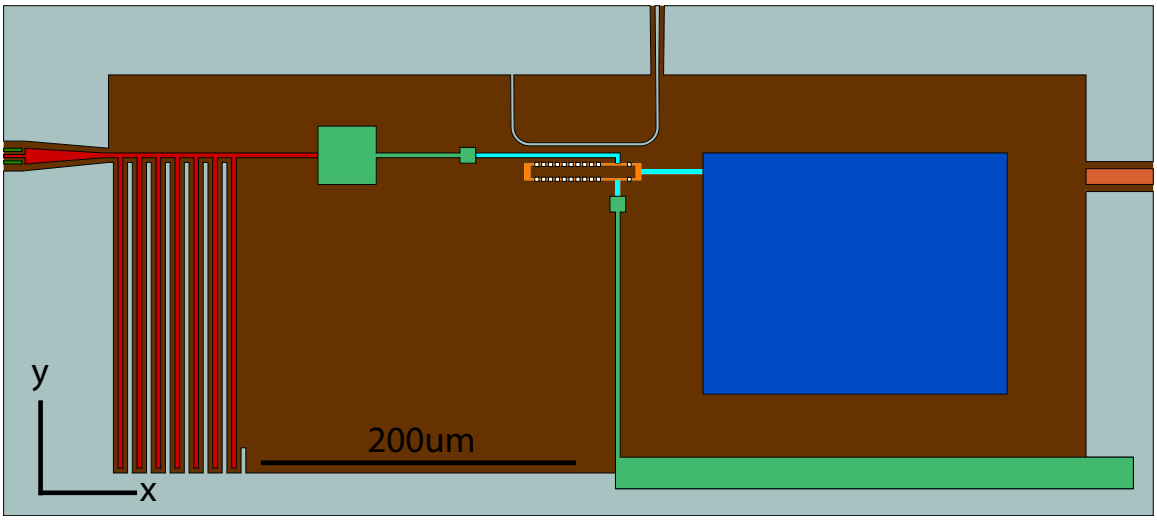

Fig. 5.14.: Closeup of the left side of the sample 4.

Table 5.9 shows the simulation results for the right and the left resonator of sample 4 for no applied magnetic field of $B = 0$ V. The simulation included the measurement result of 5.9 nH for the qubit junction inductance.
To conclude, the simulation based on the resistance measurement predicts the resonator resonance to be at ca. 5.5 GHz and the qubit at ca. 11 GHz.

5.3.3. Results from measurement round 4

A VNA measurement of the sample revealed that the left resonator on the chip was working, contrary to the right one which showed no identifiable or tunable resonance. This section

Resonator	$f_{\text{resonator}}$ [GHz]	f_{qubit} [GHz]
Left	5.275	11.06
Right	5.594	11.57

Table 5.9.: Resonator and qubit resonance frequencies for $B = 0$ V of sample 4

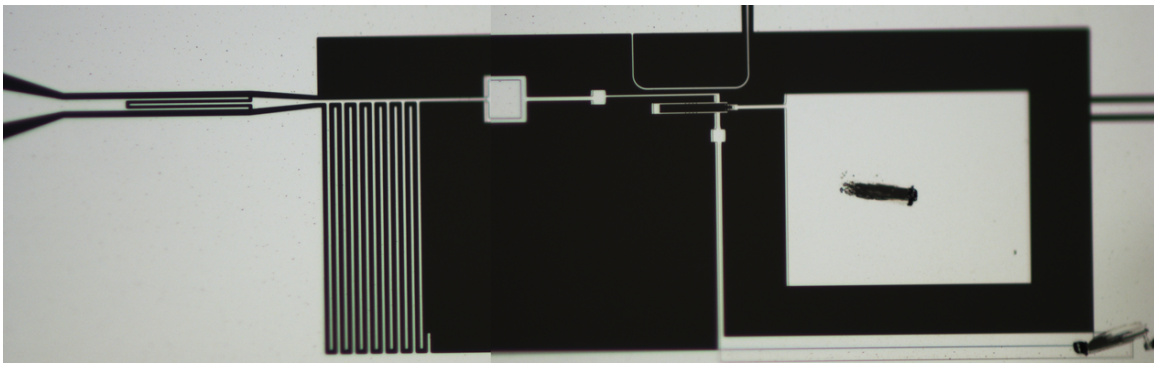

Fig. 5.15.: Optical image of the right part of sample 4

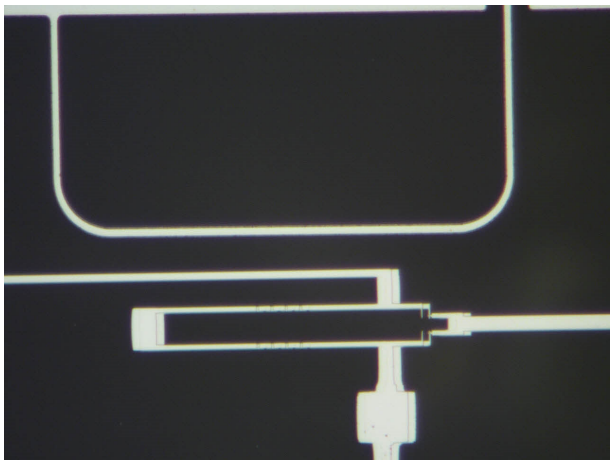

Fig. 5.16.: Closeup of the SQUIDloop with the Josephson junction array and the two qubit junctions of the right part of sample 4

therefore shows the experimental findings of the left resonator.
Figure 5.17 shows a summary of measurement round 4 as a function of applied magnetic field. The three different resonances are treated individually below.

Resonator

The resonator showed a SQUID like dependence on the applied magnetic field with a maximum frequency of 5.416 GHz, a minimum measurable frequency of 4.299 GHz and a flux offset of -0.41 flux quanta. Similar to a SQUID the slope of the resonator frequency diverged at the resonance frequency minimum. As expected from the previous cooldown, the resonator showed a red shift for increasing probing powers which is shown in Fig. 5.18a for

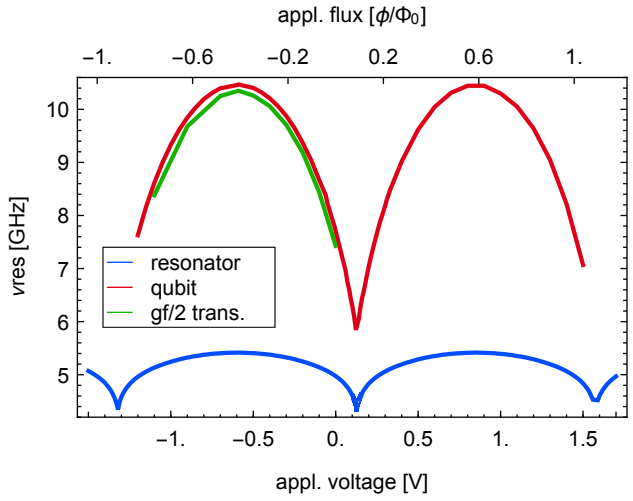

Fig. 5.17.: Summary of the frequencies as a function of magnetic field on sample 4. The resonance identified as the resonator is shown in blue, the qubit resonance in red and the higher order "gf-half transition" is depicted in green. The measurement resolution for the resonator is 0.002 V ,0.05 V for the qubit and ca. 0.2 V for the gf-half transition (cf. Fig. 5.22a).

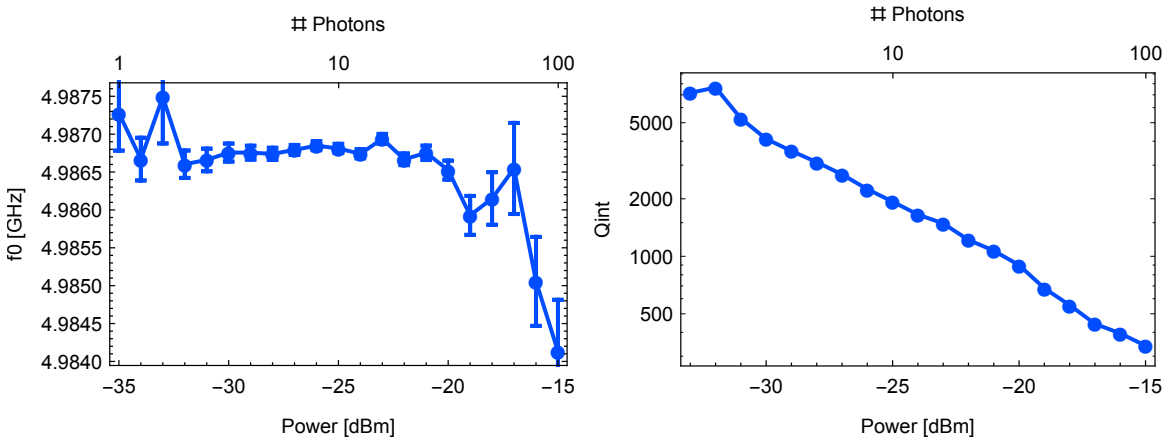

(a) Resonator resonance frequency as a function of microwave generator output power. The power at the sample is 87 dBm lower.

(b) Extracted internal quality factor Q_{int} for the resonator as a function of microwave generator output power. The power at the sample is 87 dBm lower.

Fig. 5.18.: Resonance frequency and Q_{int} of sample 4.

$B = 0$ V. The error bars for the resonance frequency fit are larger for low powers due to the noise and for high powers due to the nonlinear resonance contributions. The internal quality factor for $B = 0$ V shows a similar behavior as for measurement round 3 (Fig. 5.18b in the appendix).

Qubit

The second resonance identified as the "qubit" and colored red in Fig. 5.17 is the second degree of freedom, but can not be tuned individually as the figure shows. The periodicity as a function of magnetic field is equivalent to the periodicity of the resonator and so is the sweet spot at $B = -0.592$ V. The maximum frequency lies at 10.468 GHz and the minimum at 5.843 GHz. The qubit resonance was detected with dispersive resonator

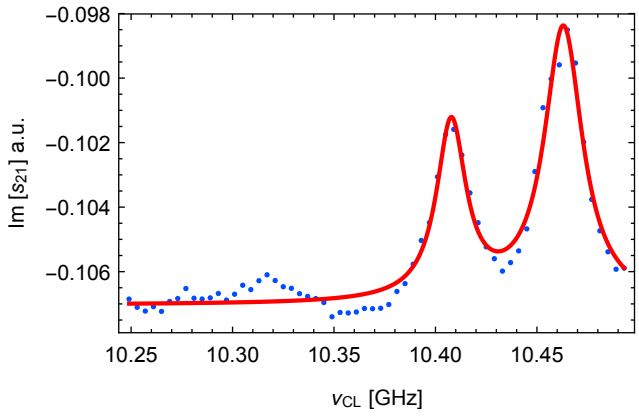

Fig. 5.19.: Dispersive resonator readout as a function of charge-line frequency at $B = -0.592$ V. The resonator was driven with -45 dBm generator power and the charge-line with -50 dBm. The red line is a two-peak Lorentzian fit.

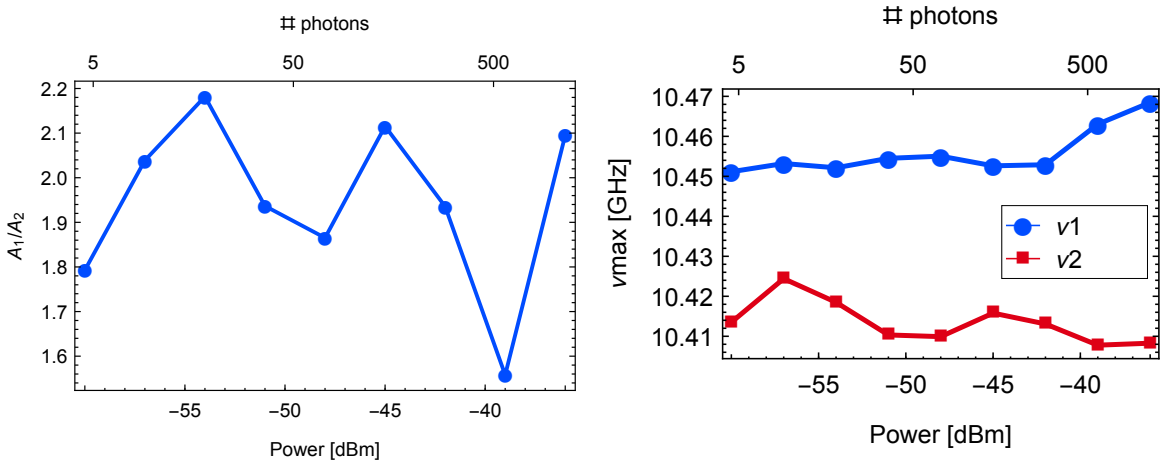

(a) Ratio of the two qubit peaks A1 (right maximal peak amplitude) to A2 (left maximal peak amplitude) in Fig. 5.21a for different resonator powers at $B = -0.592$ V. The charge line was driven with -45 dBm generator power.

(b) Power dependence of the qubit splitting for different resonator drive powers at -45 dBm charge line power drive.

Fig. 5.20.: Relative peak height $A1/A2$ and position as a function of resonator drive power.

readout although it was also observable with resonator spectroscopy if its frequency was tuned below 8 GHz (inside the observable window of the setup). However the visibility with the dispersive resonator readout was better. Figure 5.21a shows the imaginary part of the complex scattering data of the dispersive resonator readout at the sweet spot. The sweet spot is at -0.592 V coil voltage, corresponding to -0.41 flux quanta. Fig. 5.19 shows that the qubit exhibits a splitting already for -50 dBm charge line and -50 dBm resonator power which stays constant up to -35 dBm resonator power(Fig. B.5 in the appendix). The right peak which is higher in frequency is called peak 1 and the left peak which is lower in frequency is called peak 2. Both peaks show the magnetic field dependence of Fig. 5.17 and keep a constant splitting.
According to ref. [36] the relative peak height of peak 1 and 2 should change if they originate from a number state due to photons in the resonator. Figure 5.20a shows the ratio of the peak heights $A1/A2$ as a function of resonator power which fluctuates between 1.6 and 2.2, but does not decrease with increasing resonator power drive. The peaks are therefore not from number states in the resonator. The splitting of the Qubit can not be attributed to an AC Stark shift as ref. [37] suggests in combination with Fig. 5.20b. The peak splitting stays approximately constant for different resonator drive powers.
Furthermore the attempt to drive Rabi oscillations on the qubit failed. This was expected, since extracted line width of the qubit from Fig. 5.19 is ca. 20 MHz which corresponds to a coherence time of $1/(2\pi 20\text{ MHz}) < 10$ ns.

gf-half transition

If the charge line drive power is increased, higher order transitions can be driven. Fig. 5.21a and Fig. 5.21b were both measured for -45 dBm resonator drive power. As a comparison

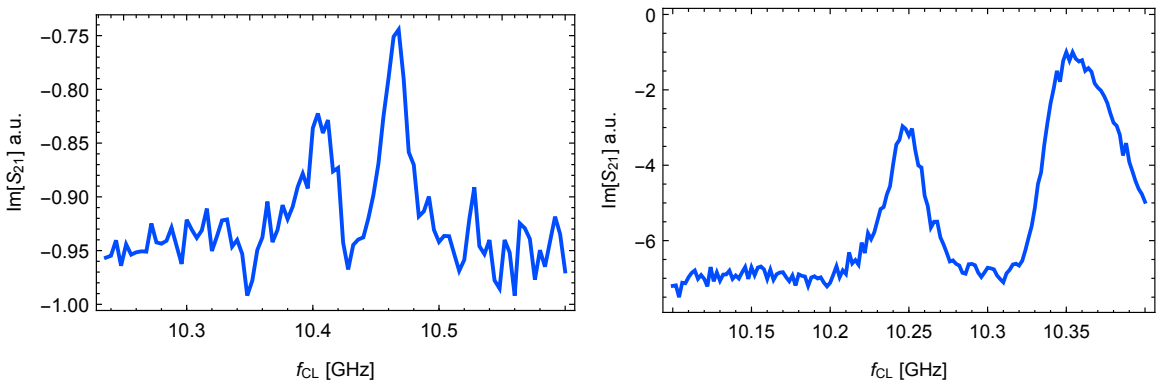

(a) Imaginary part of the scattering data of the qubit for -45 dBm charge line drive power.

(b) Imaginary part of the scattering data of the gf-half transition for -30 dBm charge line drive power.

Fig. 5.21.: Dispersive resonator readout (two tone spectroscopy) as a function of charge-line frequency at $B = -0.592$ V. The resonator was driven with -45 dBm generator power. The power at the sample was -87dBm lower.

of both figures reveals, a split peak is appearing for larger charge line drive power. This two photon transition which was assigned to the gf-half transition is 118 MHz below the qubit for $B = -0.592$ V. This split gf-half transition shows the same dependence on the magnetic field as the qubit itself which is shown in figure 5.22a. The splitting of the qubit to the gf-half transition is called the anharmonicity α which is measured as a function of applied magnetic field and shown in Fig. 5.22b. At the qubit sweet spot α is minimal and increases symmetrically for both sides of the sweet spot by approximately a factor of two. Assuming $\alpha \approx E_C$, the Josephson energy E_J can be calculated to be $24 - 50$ GHz compared to E_C of $0.27 - 0.41$ GHz. According to ref. [6] charge dispersion scales exponentially with E_J/E_C which leads to dispersion values < 1 KHz. Therefore it can be concluded that the qubit splitting does not originate from charge dispersion.
The results of measurement round 4 can be summed up as a resonator-qubit system where the qubit is split and exhibits short lifetimes. But, two photon transitions can be driven although neither photon number states nor AC Stark shift nor charge dispersion were observed.

5.3.4. Discussion of the measurement results of round 4

Table 5.10 shows the comparison of the predicted and measured resonance frequencies at the sweet spot. The resonator frequency differs by 140 MHz while the qubit differs by 590 MHz. This shows that the Josephson junction array for measurement round 4 exhibits similar properties as for round 3. Measurement round 4 was the first round in the course of this thesis where qubit Josephson junctions were tested. Therefore no experimental data is available for direct comparison which manifests itself in the larger deviation of the prediction.
The resonator frequency dependence on the magnetic field is due to the SQUID loop which

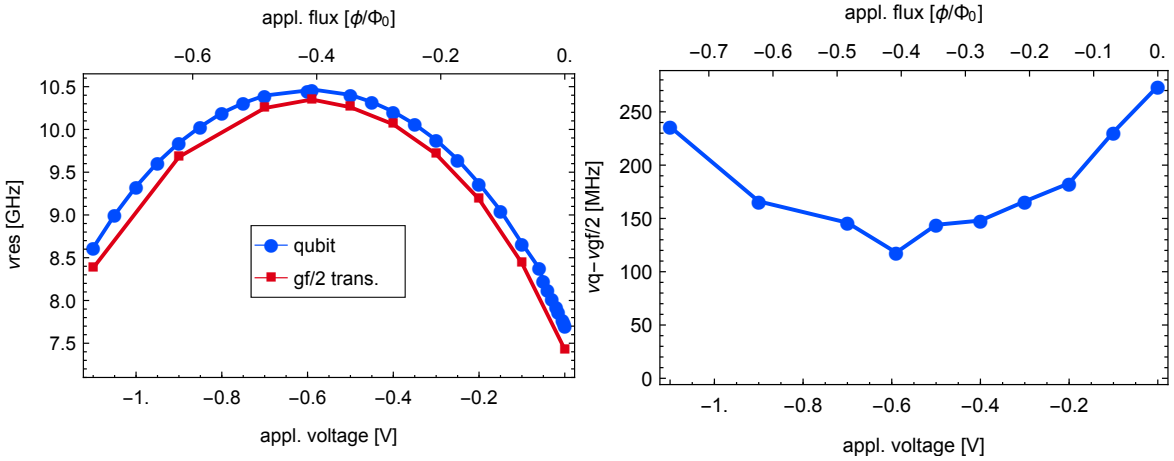

(a) Closeup of Fig. 5.17 which shows the qubit frequency and the gf-half transition frequency as a function of applied magnetic field.

(b) Power dependence of the qubit splitting for different resonator drive powers at -45 dBm charge line power drive.

Fig. 5.22.: Qubit and gf-half transition frequency and their difference α

	$f_{\text{pred.}}$ [GHz]	$f_{\text{meas.}}$ [GHz]	Δf [MHz]
Resonator	5.275	5.416	141
Qubit	11.060	10.468	592

Table 5.10.: Comparison of predicted ($f_{\text{pred.}}$) and measured ($f_{\text{meas.}}$) resonance frequencies for resonator and qubit for measurement round 4 at $B = 0$ V.

is in parallel with the Josephson junction array. A simple model is given below. The total inductance determining the resonator frequency is given by

$$L_{\text{tot}} = \frac{L_{\text{Array}} \cdot 2L_{\text{Qubit}}}{L_{\text{Array}} + 2L_{\text{Qubit}}} \tag{5.1}$$

where L_{Array} is the inductance of the Josephson junction array and L_{Qubit} the inductance of *one* Josephson junction. At the minimum resonance frequency where $L_{\text{Qubit}} \to \infty$ the approximation $L_{\text{tot}} \approx L_{\text{Array}}$ holds true. Indeed the results for the Josephson junction array resonators in table 5.5 are consistent with the minimum resonance frequency of 4.299 GHz with a deviation of ca. 150 MHz. A large tunability of the resonator can be avoided by keeping the ratio $L_{\text{Array}}/L_{\text{Qubit}} \ll 1$.

Extensive measurements on the qubit have shown that the peak splitting is not explainable with photon number states of the resonator, nor with an AC Stark shift nor with charge dispersion. This leads to the conclusion that the splitting is an intrinsic feature of this qubit. However the gf-half transition for higher charge line powers and its dependence on the magnetic field together with the behavior of α shows that the qubit resonance is indeed a higher level system. Furthermore the gf-half transition is robust for all applied magnetic fields.

The visibility of the qubit with resonator spectroscopy indicates a hybridization of the two resonances which would partly explain the short qubit lifetime.

Where is the longitudinal coupling?

Since the qubit measurements were all performed with dispersive readout, a strong transversal coupling was present and thus a weak longitudinal one as ref. [38] demonstrates. The reason why the realization proposed by ref. [25] shows no dominating longitudinal coupling lies in the way the longitudinal circuit shown in Fig. 2.1 is embedded into the experimental environment. The discussion below relies on private communications with Arne L. Grimsmo *et al.* [39].

Figure 5.23 (taken from [39]) shows two different ways of embedding the ideal longitudinal circuit of Fig. 2.1 into an experiment. As reference [39] points out the Lagrangian of circuit a) is given by

$$\begin{aligned}\mathcal{L} =& \frac{C}{2}\dot{\phi}_\mathrm{r}^2 - \frac{1}{2L}\phi_\mathrm{r}^2 \\ &+ \frac{C_{\mathrm{S1}}}{2}\left(\dot{\theta} + \frac{\dot{\phi}_\mathrm{r} - \dot{\Phi}_\mathrm{x}}{2}\right)^2 + \frac{C_{\mathrm{S2}}}{2}\left(\dot{\theta} - \frac{\dot{\phi}_\mathrm{r} - \dot{\Phi}_\mathrm{x}}{2}\right)^2 \\ &+ \frac{C_a}{2}\left(\dot{\theta} + \frac{\dot{\phi}_\mathrm{r} - \dot{\Phi}_\mathrm{x}}{2} + \dot{\phi}_1 - V_\mathrm{a}\right)^2 + \frac{C_b}{2}\left(\dot{\theta} - \frac{\dot{\phi}_\mathrm{r} - \dot{\Phi}_\mathrm{x}}{2} + \dot{\phi}_1 - V_\mathrm{b}\right)^2 \\ &+ \frac{C_1}{2}\left(\dot{\phi}_1 - V_1\right)^2 \\ &+ E_{\mathrm{J1}}\cos\left[\frac{2\pi}{\Phi_0}\left(\theta + \frac{\phi_\mathrm{r} - \Phi_\mathrm{x}}{2}\right)\right] + E_{\mathrm{J2}}\cos\left[\frac{2\pi}{\Phi_0}\left(\theta - \frac{\phi_\mathrm{r} - \Phi_\mathrm{x}}{2}\right)\right]\end{aligned} \tag{5.2}$$

where $\phi_\mathrm{r} = \phi_\mathrm{a} - \phi_\mathrm{b}$ denotes the resonator degree of freedom and $\theta = (\phi_\mathrm{a} + \phi_\mathrm{b} - \phi_1)/2$ the qubit degree of freedom. The capacitances $C_{\mathrm{S1}}, C_{\mathrm{S2}}, C_\mathrm{a}$ and C_b introduce $\dot{\theta}\dot{\phi}_\mathrm{r}$ terms which

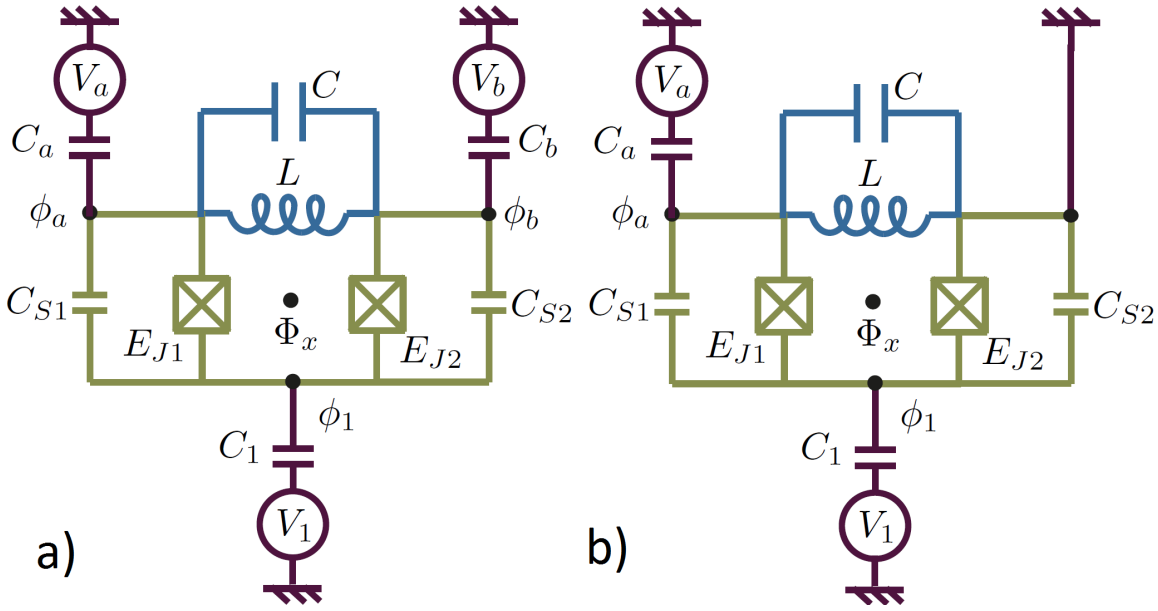

Fig. 5.23.: Two different ways of connecting the circuit of Fig. 2.1 to an experimental setup, proposed by ref. [39].

to first order is $\sigma_\mathrm{x}(a+a^\dagger)$, a transversal coupling. To cancel this coupling, the relation

$$C_{\mathrm{S1}} + C_\mathrm{a} = C_{\mathrm{S2}} + C_\mathrm{b} \tag{5.3}$$

has to be fulfilled.
The Lagrangian of circuit b) is obtained by grounding the flux node ϕ_b which leads to:

$$\begin{aligned}\mathcal{L} =& \frac{C}{2}\dot{\phi}_\mathrm{r}^2 - \frac{1}{2L}\phi_\mathrm{r}^2 \\ &+ \frac{C_{\mathrm{S1}}}{2}\left(\dot{\theta} + \frac{\dot{\phi}_\mathrm{r} - \dot{\Phi}_\mathrm{x}}{2}\right)^2 + \frac{C_{\mathrm{S2}}}{2}\left(\dot{\theta} - \frac{\dot{\phi}_\mathrm{r} - \dot{\Phi}_\mathrm{x}}{2}\right)^2 \\ &+ \frac{C_\mathrm{a}}{2}\left(\dot{\phi}_\mathrm{r} - \dot{\Phi}_\mathrm{x} - V_\mathrm{a}\right)^2 + \frac{C_1}{2}\left(\dot{\theta} - \frac{\dot{\phi}_\mathrm{r} - \dot{\Phi}_\mathrm{x}}{2} + V_1\right)^2 \\ &+ E_{\mathrm{J1}}\cos\left[\frac{2\pi}{\Phi_0}\left(\theta + \frac{\phi_\mathrm{r} - \Phi_\mathrm{x}}{2}\right)\right] + E_{\mathrm{J2}}\cos\left[\frac{2\pi}{\Phi_0}\left(\theta - \frac{\phi_\mathrm{r} - \Phi_\mathrm{x}}{2}\right)\right]\end{aligned} \tag{5.4}$$

The potential energy terms in Eq. (5.4) are equivalent to Eq. (5.2) but the kinetic terms containing the capacitances $C_{\mathrm{S1}}, C_{\mathrm{S2}}$ and C_1 play a different role. To cancel the transversal coupling, the condition

$$C_{\mathrm{S1}} = C_{\mathrm{S2}} + C_1 \tag{5.5}$$

needs to be satisfied.

Comparison of the two Lagrangians and application to the experiment

Circuit b) of Fig. 5.23 corresponds to the experimental setup of measurement round 4 (cf. Figs. 3.3,4.3) which is the lumped element realization of the proposal depicted in Fig. 2.2. The capacitance C_{S2} is equivalent to the shunt capacitance of ca. 50 fF, $C_{\mathrm{S1}} \approx 7.2$ fF consists of the Josephson junction capacitance including spurious capacitances and $C1$ is the capacitance of the charge line to the island of ca. 1 fF. Thus the condition of Eq. (5.5) is clearly not satisfied and the circuit exhibits a strong transversal coupling. Nevertheless the realized circuit topology is in principle suitable for a strong longitudinal coupling if the circuit parameters are chosen adequately.
The question of which circuits of Fig. 5.23 is to be preferred can not be answered yet because there are ongoing discussions. Circuit a) seems to exhibit the disadvantage of not protecting the qubit against direct decay into the readout line. On the other hand circuit b) has one degree of freedom less due to the grounding of ϕ_b. The influence of the grounding and the protection of the qubit decay are not yet well understood.

5.3.5. Conclusion

The experiment showed two flux tunable degrees of freedom. They are distinguishable and can be identified as a resonator and a qubit. The resonator frequency is flux tunable and matches the predicted values. The qubit is already split for low powers and exhibits a

lifetime of < 10 ns, but higher order transitions can be driven. The circuit as a whole exhibits the expected qualitative behavior such as the resonator-qubit tunability with a prediction accuracy of ca. 500 MHz. However, the origin of the qubit splitting is unknown. Furthermore the analysis has shown that the realized circuit exhibits strong transversal coupling instead of longitudinal. It revealed that the circuit parameters sensitively depend on the embedding of the circuit into the experiment.

6.Conclusion and Outlook

6.1. Conclusion

The experimental work underlying this thesis has shown that lumped element resonators with Josephson junction array inductors can be realized, however with a lower quality factors than lumped element resonators with meander inductors.
The realization proposal of ref. [25] was fabricated with a lumped element resonator and no longitudinal coupling was found. Instead a strong transversal coupling was found. The observed properties of the sample could however be qualitatively and quantitatively explained. Deeper analysis revealed the reason for the lack of longitudinal coupling. The embedding of the circuit changes the required symmetry conditions for the transversal coupling to be canceled out.
From the fabrication point of view, a process was developed which allows to produce Josephson junctions of different scales during the same electron beam lithography step.

6.2. Outlook

The next step includes the understanding of different embeddings of the longitudinal circuit into the experiment and the clarification of the question concerning the protection of the qubit against decay into the readout line.
In a second step the tunability of the resonator should be reduced by minimizing $L_{\mathrm{Array}}/L_{\mathrm{Qubit}}$ which will be a challenge from the fabrication side since the Josephson junctions will then further differ in size.
As a side project the low quality factors of lumped element resonators with Josephson junction array inductors could be improved.

7.Acknowledgments

I first thank Prof. Dr. Andreas Wallraff for giving me the opportunity to conduct my master's thesis in the QUDEV lab, which provides excellent equipment, good people and many facilities. Thank you Theo for supervising me with exceeding support, effort and advice. Thank you Philipp for effectively co-supervising me and providing steady assistance and advice. A special thank is due to Simone who put a lot of effort into the fabrication of my samples. A great thank-you belongs to the whole QUDEV group for it's constant helpfulness. It was a privilege to work with you!
An extra thank-you appertains to Jerôme, Arne and the research group of Prof. Alexandre Blais from the university of Sherbrooke for their fruitful collaboration.
My warmest appreciation belongs to my precious wife Angela who willingly incurred a lot of renouncement, especially during and after the birth of our wonderful daughter Thea. Thank you for being so affectionate and brave. I'm deeply grateful for the personal and practical support from my family and friends, especially Vlado who helped me out with the figures.
Finally, I wholeheartedly thank the one who knows that he is meant.

Bibliography

[1] A.J. Leggett, *Macroscopic quantum systems and the quantum theory of measurement*, Prog. Theor. Phys. Suppl. **69**, 80 (1980).

[2] M.H. Devoret, J.M.Martinis, and J. Clarke, *Measurements of macroscopic quantum tunneling out of the zero-voltage state of a current-biased Josephson junction*, Phys. Rev. Lett. **55**, 1908 (1985).

[3] Y. Nakamura, Yu. A. Pashkin, and J. S. Tsai, *Coherent control of macroscopic quantum states in a single-Cooper-pair box*, Nature (London) **398**, 786 (1999).

[4] J. E. Mooij *et al.*, *Josephson persistent-current qubit*, Science **285**, 1036 (1999).

[5] I. Chiorescu *et al.*, *Coherent quantum dynamics of a superconducting flux qubit*, Science **299**, 1869 (2003).

[6] J.Koch *et al.*, *Charge-insensitive qubit design derived from the Cooper pair box*, Phys. Rev. A **76**, 042319 (2007)

[7] J.A. Schreier *et al.*, *Suppressing charge noise decoherence in superconducting charge qubits*, Phys. Rev. B **77**, 180502(R) (2008).

[8] A.J. Berkley *et al.*, *Entangled macroscopic quantum states in two superconducting qubits*, Science **300**, 1548 (2003).

[9] L. DiCarlo *et al.*, *Preparation and measurement of three-qubit entanglement in a superconducting circuit*, Nature (London) **467**, 574 (2010).

[10] M. Neeley *et al.*, *Generation of three-qubit entangled states using superconducting phase qubits*, Nature (London) **467**, 570 (2010).

[11] L. DiCarlo *et al.*, *Demonstration of two-qubit algorithms with a superconducting quantum processor*, Nature (London) **460**, 240 (2009).

[12] T. Yamamoto *et al.*, *Quantum process tomography of two-qubit controlled-Z and controlled-NOT gates using superconducting phase qubits*, Phys. Rev. B **82**, 184515 (2010).

[13] E. Lucero *et al.*, *Computing prime factors with a Josephson phase qubit quantum processor*, Nat. Phys. **8**, 719 (2012).

[14] M.D. Reed *et al.*, *Realization of three-qubit quantum error correctionwith superconducting circuits*, Nature (London) **482**, 382 (2012).

[15] A. Blais *et al.*, *Cavity quantum electrodynamics for superconducting electrical circuits: An architecture for quantum computation*,Phys. Rev. A **69** ,062320 (2004)

[16] E. Jeffrey *et al.*, *Fast Accurate State Measurement with Superconducting Qubits*, Phys. Rev. Lett. **105**m 190504 (2014)

[17] A.A. Houck *et al.*, *Controlling the Spontaneous Emission of a Superconducting Trans-*

mon Qubit, Phys.Rev. Lett. **101**, 080502 (2008).

[18] D. Leibfried *et al.*, *Experimental demonstration of a robust, high-fidelity geometric two ion-qubit phase gate*, Nature, **422** 412-5 (2003)

[19] P.C. Haljan *et al.*, *Spin-Dependent Forces on Trapped Ions for Phase-Stable Quantum Gates and Entangled States of Spin and Motion*, Phys. Rev. Lett. **94**, 153602 (2005)

[20] K. MÃ¸lmer and Anders Sørensen, *Multiparticle Entanglement of Hot Trapped Ions*, Phys. Rev. Lett. **82**, 1835-8 (1999)

[21] A. Sørensen and K. Mølmer, *Entanglement and quantum computation with ions in thermal motion*, Phys. Rev. A **62** 022311 (2000)

[22] G.J. Milburn, S. Schneider and D.F.V. James, *Ion trap quantum computing with warm ions*, Fortschr. Phys. **48**, 801-10 (2000)

[23] A.J. Kerman, *Quantum information processing using quasiclassical electromagnetic interactions between qubits and electrical resonators*, New J. Phys. **15**, 123011 (2013)

[24] P.-M. Billangeon, J. S. Tsai, and Y. Nakamura,Circuit-QED-based scalable architectures for quantum information processing with superconducting qubits , Phys. Rev. B **91**, 094517 (2015).

[25] N. Didier, J. Bourassa and A. Blais., *Fast quantum non-demolition readout from longitudinal qubit-oscillator interaction*, Phys. Rev. Lett., 115:203601 (2015)

[26] M.H. Devoret, *Quantum fluctuations in electrical circuits*, Les Houches, Session LXIII, (1995)

[27] E.T. Jaynes, F.W. Cummings, *Comparison of quantum and semiclassical radiation theories with application to the beam maser*, Proc. IEEE 51 (1): 89-109 (1963)

[28] Y. Makhlin, G. Schön, A. Shnirman, *Quantum-state engineering with Josephson-junction devices*, Rev. Mod. Phys. **73**, 357 (2001).

[29] J. Bourassa *et al.*, *Josephson-junction-embedded transmission-line resonators: From Kerr medium to in-line transmon*, Phys. Rev. A **86**, 013814 (2012)

[30] J. Gambetta *et al.*, *Quantum trajectory approach to circuit QED: Quantum jumps and the Zeno effect*,Phys. Rev. A **77**, 012112 (2008)

[31] S. Probst *et al.*, *Efficient and robust analysis of complex scattering data under noise in microwave resonators*, Rev. Sci. Instrum. **86**, 024706 (2015)

[32] K. Geerlings *et al.*, *Improving the quality factor of microwave compact resonators by optimizing their geometrical parameters*, Appl. Phys. Lett.**100**, 192601 (2012)

[33] C. Wang *et al.*, *Surface participation and dielectric loss in superconducting qubits*, Appl. Phys. Lett.**107**, 162601 (2015)

[34] S. Burkhard, *Optimization of transmon design for longer coherence time*, Semesterthesis Qudev Group, Spring Semester 2012

[35] G. Stojanovic, Ljiljana Zivanov and Mirjana Damnjanovic, *Novel efficient methods for inductance calculation of meander inductor*, IEEE Vol. **25** No. 4 (2006)

[36] D.I. Schuster *et al.*, *Resolving photon number states in a superconducting circuit*, Nature, (London), **445** 05461 (2007)

[37] A. Wallraff *et al.*, *Sideband Transitions and Two-Tone Spectroscopy of a Superconducting Qubit Strongly Coupled to an On-Chip Cavity*, Phys. Rev. Lett. **99**, 050501 (2007)

[38] S. Richer and D. DiVincenzo, *Circuit design implementing longitudinal coupling: A scalable scheme for superconducting qubits*, Phys. Rev. B **93** ,134501 (2016)

[39] A.L. Grimsmo, *Lumped Element Circuits for Longitudinal Coupling*, unpublished (2016)

[40] A. Potocnik, *Lumped Element Oscillator Arrays for Quantum Simulation Experiments*, internal document, unpublished.

A.Detailed discussion of measurement round 1 and 2

A.1. Cooldown 1

A.1.1. Sample for measurement round 1 (sample 1)

Purpose

The purpose of sample 1 was to investigate the influence of the floating ground and the other components of the floating version for five different resonators and to measure Q_{int} of these resonators with a weak external coupling of 40 KHz. The resonators are arranged on the chip such that they can be read out as a notch type circuit (cf. ref. [31]) which allows for the extraction of the external and internal quality factor. A schematic of sample 1 is shown in Fig. A.1. This sample was aimed to be a resonator test and did thus not contain any qubit junctions.

Description of the sample design

The five resonators shown in Fig. A.1 have five different resonance frequencies. The inductance given by the Josephson junction array was kept constant at $L \approx 4.6$ nH, while the capacitance was varied. Figure A.2 shows the result of 5 different finger capacitor simulations with a linear fit. These are the non-renormalized capacitances $C_{\text{res-fltgnd}}$. The following table A.1 summarizes the simulated results and compares them to experimentally predetermined values for finger capacitors from [40]. The capacitance simulations were performed with Maxwell and the resonance frequencies were determined with Microwave Office based on the model shown in Fig. 3.1 with the decoupled qubit circuit. According to the simulations, the properties of the resonators were chosen as shown in table A.1. The fourth column lists the spurious capacitance C_{spur} of the resonator to ground and the fifth column the renormalized capacitances C_{ren} as discussed in section 3.4.
The coupling of the resonators to the transmission line was realized capacitively with a gap of 100 μm as schematically depicted in Fig. A.3. The oscillator damping rate κ not only

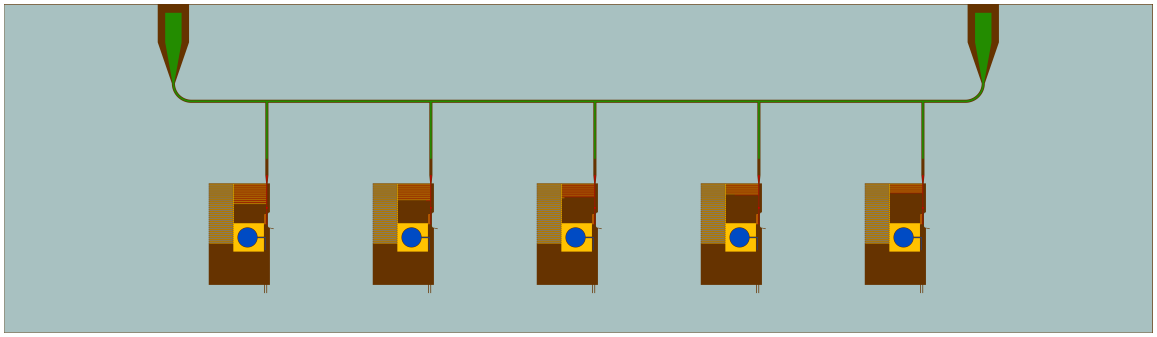

Fig. A.1.: Schematic of sample 1. The five resonators are coupled capacitively to the transmission line (green). No charge and no flux-line were added.

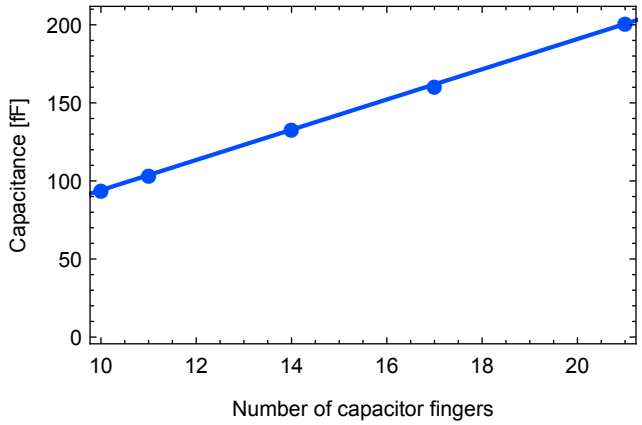

Fig. A.2.: Simulated capacitances $C_{\mathrm{res-fltgnd}}$ as a function of number of capacitor fingers with linear regression line

Resonator	# fingers	C_{ref} [fF] [40]	C_{sim} [fF]	C_{spur} [fF]	C_{ren} [fF]	f_{res} [GHz]
1	21	218	201	43	230	4.884
2	17.1	177	163	42	201	5.225
3	14	144	133	42	174	5.614
4	11.7	119	111	38	149	6.063
5	10	101	94	41	135	6.368

Table A.1.: Resonator number (from left to right) with corresponding finger number, reference capacitance from previous measurements C_{ref}, capacitance to floating ground C_{sim}, spurious capacitance to ground C_{spur} and renormalized capacitance C_{ren} for $L_{\mathrm{res}} = 4.6$ nH and 100 μm coupling capacitor gap size. The last column shows the expected resonance frequencies for C_{ren}, determined with Microwave Office.

depends on the coupling capacitor C_{coupl}, but also on the resonator capacitor. Table A.2 shows an overview of the coupling rate κ for different resonator capacitors C_{res} and coupling capacitor gap sizes.

		$\kappa/2\pi$ [MHz] for $C_{\mathrm{res}} = \ldots$ [fF]				
Gap [μm]	C_{coupl} [fF]	230	201	174	149	135
100	0.77	0.019	0.025	0.034	0.046	0.056
60	1.44	0.067	0.088	0.117	0.159	0.193
50	1.53	0.076	0.099	0.132	0.179	0.218
30	1.74	0.098	0.128	0.170	0.231	0.281
10	4.34	0.595	0.807	1.070	1.392	1.686
5	6.95	1.494	1.941	2.566	3.458	4.176

Table A.2.: Different κ as a function of capacitor gap size and resonator capacitor.

For table A.2 κ was determined by fitting a Lorentzian to the simulated response function of the model shown in Fig. 3.1 which for the present sample is between $\kappa/2\pi = 19$ KHz and $\kappa/2\pi = 56$ KHz.

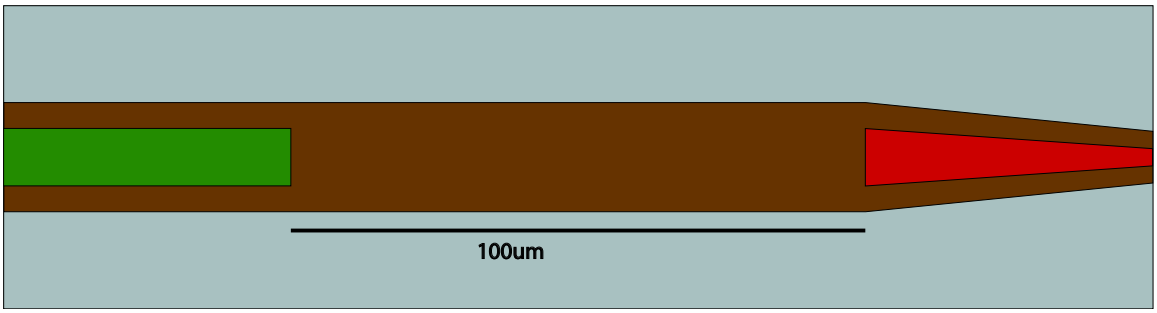

Fig. A.3.: Coupling capacitor of sample 1

Peculiarities of the first sample

Since this sample was aimed for a test of the resonance frequencies and Q_{int} of the resonators, no qubit and thus no charge and flux-line were added. This was realized by not writhing the two Josephson junctions connecting the junction array with the island. An optical image of this situation is shown in Fig. A.4 (cf. Fig. 3.4). The island is therefore unconnected and floating.

A.1.2. Sample examination after fabrication

Finger thickness

An antecedent sample examination revealed that all structures written by electron beam lithography were 1.2 μm thicker in $x-$direction than expected as shown in Fig. A.5. This effect originated from the fact that during the electron beam lithography two layers of aluminum are deposited with two different angles of $\pm 45^o$. This causes the structures in one direction to be larger by twice the thickness of the deposited layer which is ca. 600 nm. The increased finger thickness caused a larger capacitance. Microwave Office simulations were performed to estimate the new resonance frequencies.
In addition the resistance of one Josephson junction array was measured to be ca. 4.2k Ω

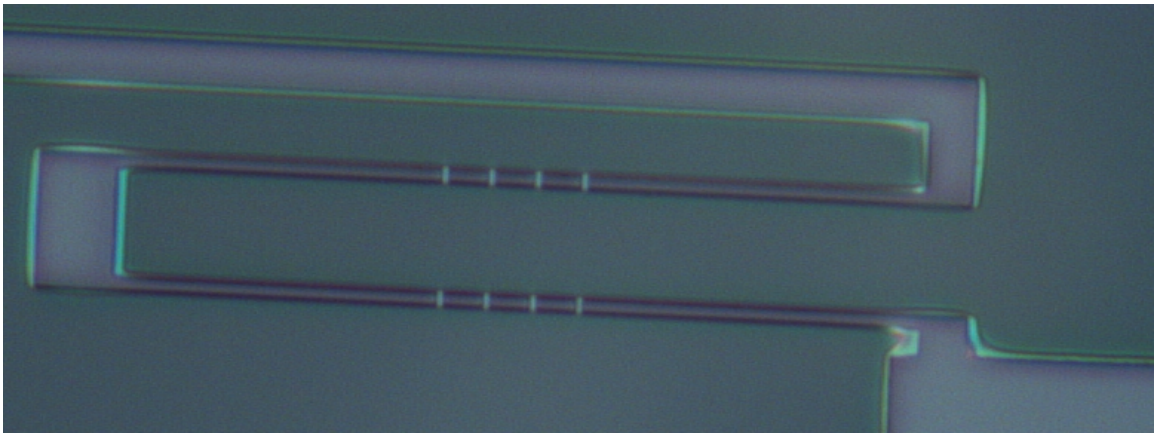

Fig. A.4.: Optical image of the Josephson junction array

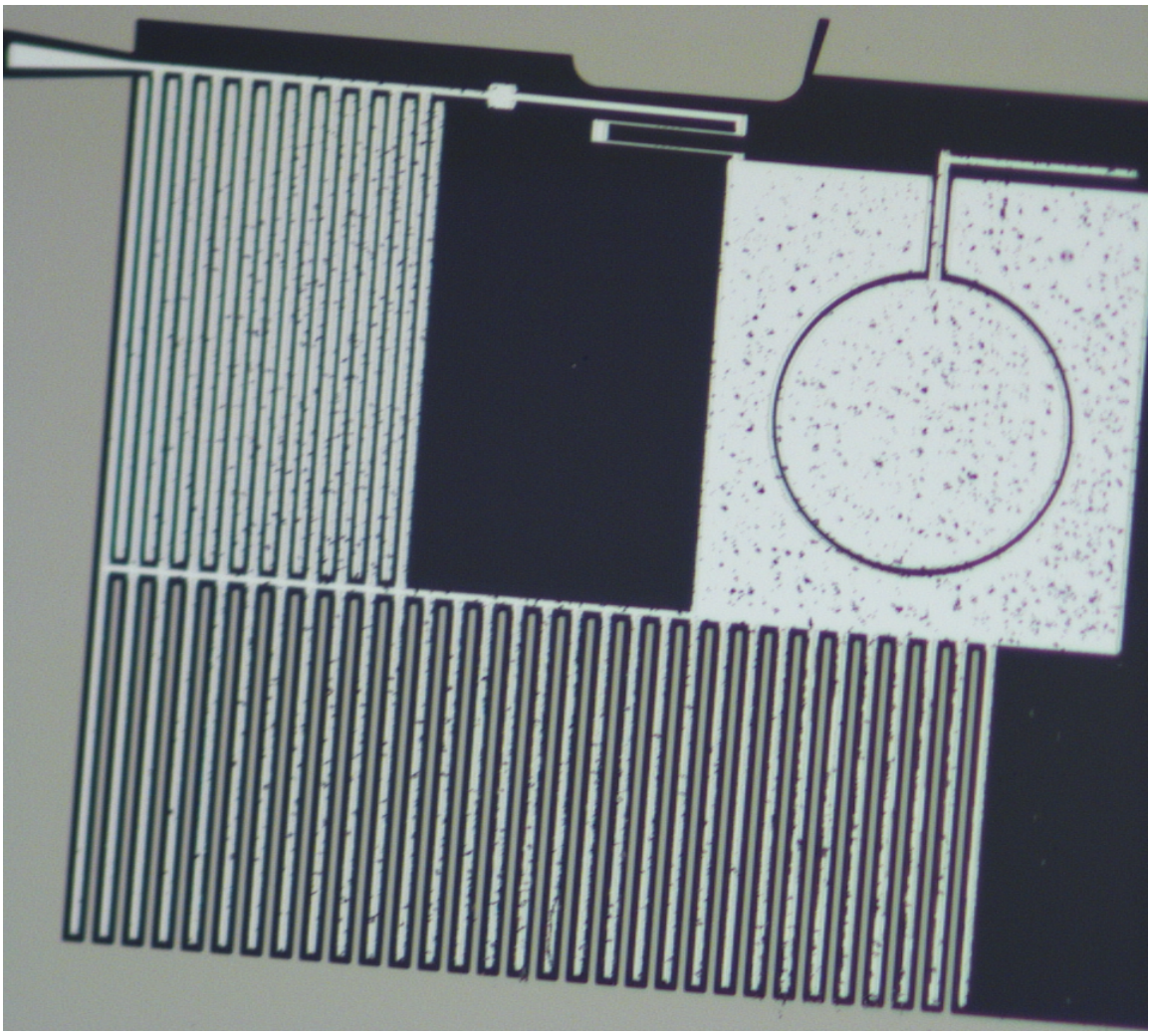

Fig. A.5.: Optical image of resonator 1 of sample 1.

which allows one to determine the inductance of 4.9 nH. Table A.3 shows the modified capacitances and the expected resonance frequencies. The measurement of the resistance most likely destroyed one resonator by shorting the resonator capacitor.

Resonator	$C_{\mathrm{res,thick}}$ [fF]	L_{res} [nH]	f_{res}
1	306	4.9	4.105
2	260	4.9	4.453
3	223	4.9	4.806
4	195	4.9	5.139
5	175	4.9	5.423

Table A.3.: Resonance frequency expectation stemming from the modified resonator capacitor due to the thicker fingers and the increased junction array inductance.

Quality factor

Furthermore the optical examination of Fig. A.5 shows that the sample is very dirty which most likely will lead to a low $Q_{\mathrm{int}}/Q_{\mathrm{L}}$.

A.1.3. Results and discussion

The resonators themselves were measured in reflection, but the whole chip (cf. e.g. fig A.1) was measured in transmission with a vector network analyzer (VNA). The sample was probed for different VNA output powers in the range of $3.8-8.5$ GHz with an IF bandwidth of 30 KHz, but no distinct resonances were observed. The measurement setup appeared to be working, for example the power transition depended on the HEMT power and the signal shape showed the characteristics of the $4-10$ GHz bandpass filter.
The phase measurement revealed for small resonances which could not be observed in amplitude or in the complex plane. The phase fit yielded the parameters shown in table A.4. These four spurious resonances are discussed in more detail in section A.2 about cooldown 2 since they were observed there as well.

	f_{res} [GHz]	Q_{l}	Q_{c}
Resonance 1	4.00649	3000	165'000
Resonance 2	4.35020	3900	233'000
Resonance 3	4.66444	4000	181'000
Resonance 4	4.94789	4700	161'000

Table A.4.: Phase fit parameters for the four observed resonances.

The results of measurement round 3 (section 5.2) suggest that the coupling of the resonators to the transmission line was overestimated which impeded together with the low sample quality the observation of the resonances.

A.2. Cooldown 2

A.2.1. Sample for measurement round 2 (sample 2)

Purpose

The purpose of the second sample was identical with the first one described in section A.1.1. Changes comprised an increase of κ for a better resonance visibility and thinned capacitor fingers.

Description of the sample design

For the second sample the coupling of the resonators to the transmission line was changed. This was realized through a variation of the coupling capacitor gap size schematically depicted in Fig. A.3. The results shown in table A.2 lead to the choice displayed in table A.5.

Resonator Nr.	C_{res} [fF]	Gap [μm]	$\kappa/2\pi$ [KHz]	f_{res} [GHz]
1	230	30	98	4.874
2	201	10	807	5.179
3	174	30	170	5.597
4	149	10	1392	5.993
5	135	30	281	6.345

Table A.5.: Resonator number (from left to right as in Fig. A.1) and corresponding coupling/gap size and expected resonance frequency f_{res} for the resonators on the chip for the second cooldown. The different coupling capacitors lead to slightly different resonance frequencies compared to sample 1.

Thinned capacitor fingers

The analysis of the first sample revealed that all structures written with electron beam lithography were in $x-$direction 1.2 μm thicker than expected. A detailed description of this is found in section A.1.2. To compensate for this effect, the finger thickness of the finger capacitor was reduced to 1.8 μm.

A.2.2. Sample examination after fabrication

Optical examination of the sample

An optical examination of the second sample shows, that the compensation for the finger thickness was successful. Figure A.6 shows resonator 1 of sample 2. The sample is still not very clean, but the fingers of the capacitors are regularly spaced. The Josephson junction array is misaligned with respect to the rest of the structure due to the different writing field for the Josephson junctions. The island is still not connected as desired and for this reason it was not compensated for the thickening in $x-$direction.

Resistance measurement

The Josephson junction arrays for sample 2 were fabricated with exactly the same parameters as for the first sample. Therefore the resistance of the junction arrays was expected to be again 4.2 kΩ which corresponds to an inductance of 4.9 nH. Table A.6 shows the adjusted expectation for the resonance frequencies of sample 2.

Resonator	C_{res}	Gap [μm]	$\kappa/2\pi$ [MHz]	f_{res} [GHz]
1	230	30	98	4.723
2	201	10	807	5.018
3	174	30	170	5.424
4	149	10	1392	5.806
5	135	30	281	6.148

Table A.6.: Adjusted resonance frequency expectation for sample 2 with $L_{\text{res}} = 4.9$ nH.

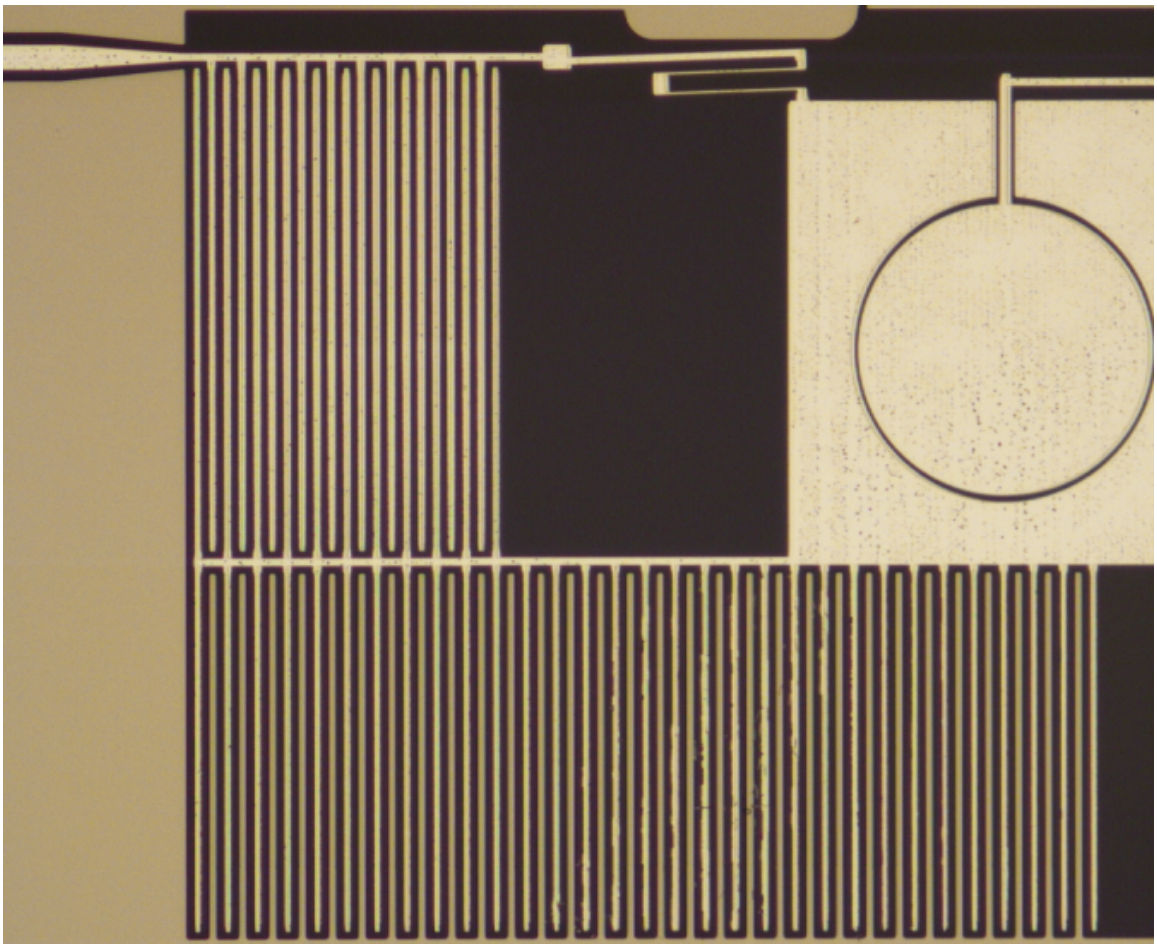

Fig. A.6.: Optical image of resonator 1 of sample 2.

A.2.3. Results from measurement round 2

Sample 2 was measured in an analogous way to sample 1 in transmission between 3.7 and 8.7 GHz. The amplitude did not reveal any resonances. In the phase quadrature 4 resonances were observed. A phase fit of the notch geometry of Eq. (2.25) yielded the following parameters shown in table A.7.

	f_{res} [GHz]	Q_{l}	Q_{c}
Resonance 1	3.969	3121	124071
Resonance 2	4.324	2175	146408
Resonance 3	4.652	1856	164398
Resonance 4	4.964	3249	362629

Table A.7.: Fit parameters for sample 2 measurement.

A.2.4. Discussion

An examination of the fitted resonance frequencies reveals the striking fact that they do heavily differ from the expected values shown in table A.6, but are almost equivalent to the results of the previous measurement of sample 1.

$f_{\mathrm{res},1}$[GHz]	$f_{\mathrm{res},2}$ [GHz]	$\Delta_{12} f_{\mathrm{res}}$ [MHz]
4.006	3.969	36.6
4.352	4.324	27.8
4.664	4.652	11.8
4.948	4.964	-16.4

Table A.8.: Comparison of the results of the first and second measurement round and their difference.

Sample examination after warm up

A resistance measurement performed on all resonators after the sample was removed from the cryostat showed resistances of ca. 4.2k Ω for all junction arrays. The resistance matches the expected resistance for the desired inductance of the junctions. The images of the resonators were checked carefully for shorts or irregularities which may have affected the resonators, but none were found.

A.2.5. Conclusion

With only a small differences same resonances were measured in samples 1 and 2, although the capacitors of the resonator were changed by a capacitance of ca. 40 fF. This leads to the conclusion that these resonances are not the designed ones and were just spurious resonances. A careful examination of all coplanar waveguide distances on the chip did not show any coincidence with the observed resonances. Additionally a subsequent dipstick measurement of the sample showed no resonances which implies that the resonances do not stem from standing waves in the coplanar waveguide lines of the chip. During measurement round 3 these four resonances were not observed which suggest that they are a peculiar property of the first two samples, since they could not be observed, neither for the floating nor for the grounded version. Thus it may be concluded that the occurrence of these resonances correlates with the non-observability of the resonator resonances. Further investigations on this topic are needed to fully explain the results.

B. Supplementary graphs and tables

B.1. Simulations for sample 3a

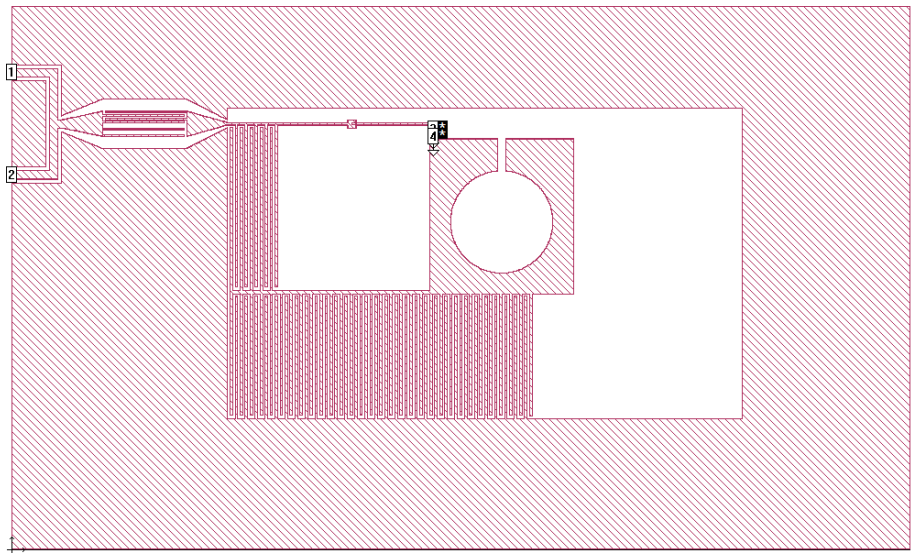

Fig. B.1.: Sonnet simulation geometry. Resonator 5 of the floating version of sample 3 is shown.

Res.	C [fF]	L [nH]	$f_{\mathrm{r,M}}$[GHz]	$f_{\mathrm{r,S}}$[GHz]	$\frac{\kappa_{\mathrm{M}}}{2\pi}$ [MHz]	$\frac{\kappa_{\mathrm{S}}}{2\pi}$ [MHz]	Δf_{r}[MHz]
1	230	4.12	4.932	5.382	15.5	3.7	450
2	201	4.6	4.961	5.203	17.7	4.4	242
3	230	4.6	4.669	4.663	13.9	5.7	-6
4	149	4.12	5.982	6.473	33.8	7.4	491
5	135	4.6	5.909	5.956	35.9	8.5	47

Table B.1.: Overview of resonator capacitances, inductances, resonance frequencies and coupling rates κ of the 5 resonators implemented on the sample 3a. The resonance frequencies and coupling rates κ were simulated with Microwave Office ($f_{\mathrm{r,M}}, \kappa_M$) and with Sonnet ($f_{\mathrm{r,S}}, \kappa_S$). Resonator 3 is tunable due to the SQUID array inductor and the table thus displays the aimed sweet spot values.

The two simulations coincide for the resonance frequencies prediction for resonator 3 and 5 and differ by ca. 0.5 GHz for resonators 1 and 4. This deviation can be explained by an overestimation of the inductance of the meandering line. Indeed reference [35] reports an error of maximally 12% for the equation they deliver to calculate the inductance. This would explain ca. 300 MHz of the deviation. The origin of deviation of the two simulations for resonator 2 could not be elicited. However a deviation of the two types of simulation is expected since pure lumped element model does not account for geometrical effects in the microwave regime. However it is striking that the simulations for κ differ that much. The experiment (measurement round 3) described in section 5.2 shows that the Sonnet simulations are much closer which again is expected due to neglected geometrical effects of in Microwave Office.

B.2. Simulations for sample 3b

Figure B.2 shows the simulated capacitances of the resonator to ground for 5 different finger numbers. It is interesting that the capacitances are indeed larger than for the floating version shown in Fig. A.2. But if the renormalized capacitance (e.g. cf. table A.1) is compared to these results, they do match what is expected (cf. section 3.4).
Table B.2 shows an overview of the expected resonance frequencies and coupling rates κ based on the finger capacitor capacitance C_{sim} and inductors L_{ind}. The resonance frequencies were simulated once with the lumped element model depicted in Fig. 3.1 and with Sonnet based on the actual sample geometry shown in Fig. 5.3. The coupling rates κ were extracted by fitting a Lorentzian to the response function in both cases. As for the grounded version, the Sonnet simulations were also performed in a notch type geometry (cf. Fig. B.1). The Microwave Office and Sonnet simulations deviate by ca. 150 MHz for the SQUID array inductor type and by ca. 580 MHz for the meander inductor type. An overall deviation between the two models is expected and the large deviation in case of the meander inductor originates from an overestimate of the inductance of the meander inductor. Again, as for the floating version, a significant deviation in κ is exhibited however smaller. Interestingly the experiments seems to support the Microwave Office simulation in this case (cf. section 5.2).

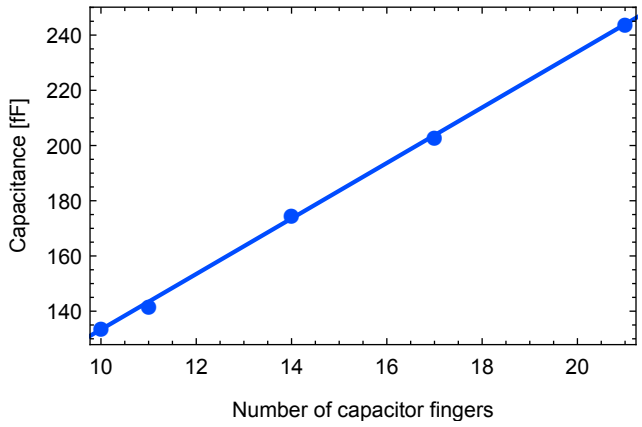

Fig. B.2.: Simulated capacitances $C_{\mathrm{res-gnd}}$ as a function of number of capacitor fingers with linear regression line for the grounded version

Res.	L [nH]	C [fF]	$f_{\mathrm{r,M}}$[GHz]	$f_{\mathrm{r,S}}$[GHz]	$\frac{\kappa_{\mathrm{M}}}{2\pi}$ [MHz]	$\frac{\kappa_{\mathrm{S}}}{2\pi}$ [MHz]	Δf_{r}[MHz]
1	4.12	244	4.893	5.474	4.8	1.8	581
2	4.12	205	5.313	5.899	6.6	2.7	586
3	4.6	174	5.430	5.543	8.1	2.2	113
4	4.6	150	5.816	5.969	10.6	8.7	153
5	4.6	133	6.146	6.318	13.3	1.3	172

Table B.2.: Overview of the grounded version of sample 3 with finger number, capacitance C, inductance L, simulated resonance frequency $f_{\mathrm{r,M}}$ and $f_{\mathrm{r,S}}$ and the coupling rate $\kappa_{M,S}$ where the subscript M denotes the Microwave Office Simulation and S the Sonnet simulation.

B.3. Supplementary results of measurement round 3

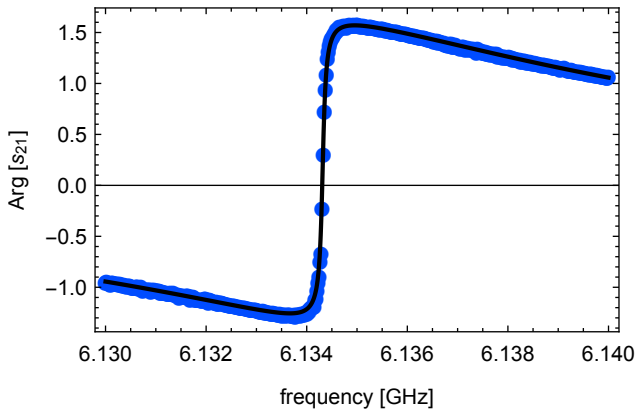

Fig. B.3.: Phase data and fit of the fourth resonator on the sample 3a with a meander inductor. The data was taken for $B = 0$ V and -77 dBm sample power.

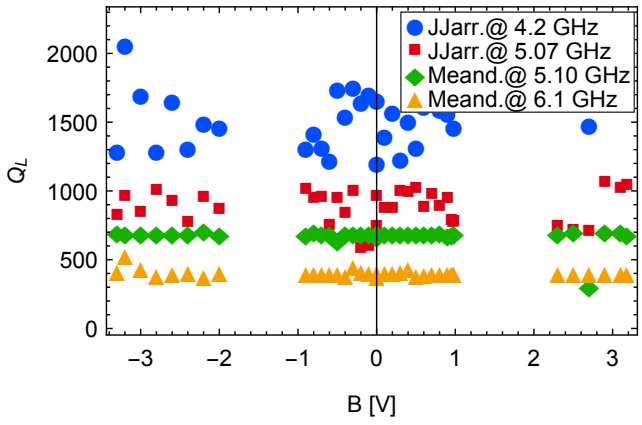

Fig. B.4.: Bfield dependence of the loaded quality factors of the resonators on sample 3a

B.4. Supplementary results of measurement round 4

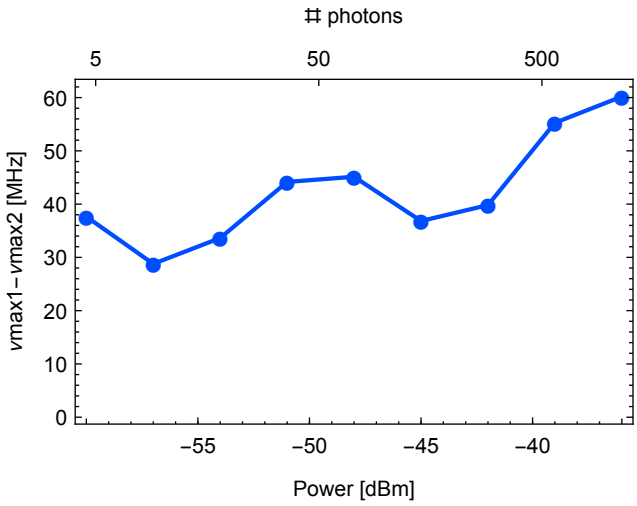

Fig. B.5.: Splitting of the qubit resonance for $B = 0$ V and -32 dBm charge-line power as a function of resonator drive power

Eidgenössische Technische Hochschule Zürich
Swiss Federal Institute of Technology Zurich

Declaration of originality

The signed declaration of originality is a component of every semester paper, Bachelor's thesis, Master's thesis and any other degree paper undertaken during the course of studies, including the respective electronic versions.

Lecturers may also require a declaration of originality for other written papers compiled for their courses.

I hereby confirm that I am the sole author of the written work here enclosed and that I have compiled it in my own words. Parts excepted are corrections of form and content by the supervisor.

Title of work (in block letters):

Towards the realization of a transmon longitudinally coupled to a lumped element resonator

Authored by (in block letters):
For papers written by groups the names of all authors are required.

Name(s):	**First name(s):**
Beckert	Adrian

With my signature I confirm that

- I have committed none of the forms of plagiarism described in the 'Citation etiquette' information sheet.
- I have documented all methods, data and processes truthfully.
- I have not manipulated any data.
- I have mentioned all persons who were significant facilitators of the work.

I am aware that the work may be screened electronically for plagiarism.

Place, date	**Signature(s)**
Zürich, 21.04.2016	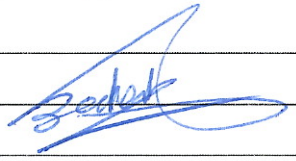

For papers written by groups the names of all authors are required. Their signatures collectively guarantee the entire content of the written paper.